SUBMISSION : APRIL 24, 2014, ACCEPTED : SEPTEMBER 16, 2014
Preprint typeset using LaTeX style emulateapj v. 04/17/13

arXiv:1404.6066v2 [astro-ph.CO] 19 Sep 2014

ACCELERATED EVOLUTION OF THE Lyα LUMINOSITY FUNCTION AT $z \gtrsim 7$ REVEALED BY THE SUBARU ULTRA-DEEP SURVEY FOR Lyα EMITTERS AT $z = 7.3$

AKIRA KONNO[1,2], MASAMI OUCHI[1,3], YOSHIAKI ONO[1], KAZUHIRO SHIMASAKU[2,4], TAKATOSHI SHIBUYA [1,5], HISANORI FURUSAWA [6]
KIMIHIKO NAKAJIMA[2], YOSHIAKI NAITO [1], RIEKO MOMOSE[1], SURAPHONG YUMA [1] AND MASANORI IYE [6]

Submission : April 24, 2014, Accepted : September 16, 2014

ABSTRACT

We present the ultra-deep Subaru narrowband imaging survey for Lyα emitters (LAEs) at $z = 7.3$ in SXDS and COSMOS fields (~ 0.5 deg^2) with a total integration time of 106 hours. Exploiting our new sharp bandwidth filter, *NB101*, installed on Suprime-Cam, we have reached $L(\mathrm{Ly}\alpha) = 2.4 \times 10^{42}$ erg s^{-1} (5σ) for $z = 7.3$ LAEs, about 4 times deeper than previous Subaru $z \gtrsim 7$ studies, which allows us to reliably investigate the evolution of the Lyα luminosity function (LF), for the first time, down to the luminosity limit same as those of Subaru $z = 3.1 - 6.6$ LAE samples. Surprisingly, we only find three and four LAEs in SXDS and COSMOS fields, respectively, while one expects a total of ~ 65 LAEs by our survey in the case of no Lyα LF evolution from $z = 6.6$ to 7.3. We identify a decrease of the Lyα LF from $z = 6.6$ to 7.3 at the $> 90\%$ confidence level from our $z = 7.3$ Lyα LF with the best-fit Schechter parameters of $L^*_{\mathrm{Ly}\alpha} = 2.7^{+8.0}_{-1.2} \times 10^{42}$ erg s^{-1} and $\phi^* = 3.7^{+17.6}_{-3.3} \times 10^{-4}$ Mpc^{-3} for a fixed $\alpha = -1.5$. Moreover, the evolution of the Lyα LF is clearly accelerated at $z > 6.6$ beyond the measurement uncertainties including cosmic variance. Because no such accelerated evolution of the UV-continuum LF or the cosmic star-formation rate (SFR) is found at $z \sim 7$, but suggested only at $z > 8$ (Oesch et al. 2013; Bouwens et al. 2014), this accelerated Lyα LF evolution is explained by physical mechanisms different from a pure SFR decrease but related to the Lyα production and escape in the process of cosmic reionization. Because a simple accelerating increase of IGM neutral hydrogen absorbing Lyα would not reconcile with Thomson scattering optical depth measurements from *WMAP* and *Planck*, our findings may support new physical pictures suggested by recent theoretical studies, such as the existence of HI clumpy clouds within cosmic ionized bubbles selectively absorbing Lyα and the large ionizing photon escape fraction of galaxies making weak Lyα emission.

Keywords: cosmology: observations — dark ages, reionization, first stars — galaxies: formation — galaxies: high-redshift — galaxies: luminosity function, mass function

1. INTRODUCTION

Lyα emitters (LAEs) are young star-forming galaxies, and are essential to explore very high redshift universe. A large number of systematic narrowband imaging surveys have been carried out for LAEs at $z \sim 7$ (Iye et al. 2006; Ota et al. 2008, 2010; Shibuya et al. 2012) and beyond $z \sim 8$ (Willis & Courbin 2005; Cuby et al. 2007; Willis et al. 2008; Sobral et al. 2009; Hibon et al. 2010; Tilvi et al. 2010; Clément et al. 2012; Krug et al. 2012; Matthee et al. 2014). In these studies, it is under debate whether the Lyα luminosity function (LF) of LAEs evolve from $z = 6.6$ or not, while no evolution of the Lyα LF in $z = 3.1 - 5.7$ (Ouchi et al. 2008) and a decrease from $z = 5.7$ to 6.6 (Kashikawa et al. 2006, 2011; Ouchi et al. 2010; Hu et al. 2010) have been identified. Hibon et al. (2010), Tilvi et al. (2010) and Krug et al. (2012) conclude that there is no evolution of the Lyα LF from $z = 6.6$ to 7.7. On the other hand, Clément et al. (2012) place the upper limit on the Lyα LF based on their result of no detection of $z = 7.7$ LAE, and rule out no evolution of the Lyα LF in $z = 6.6 - 7.7$. Moreover, the observations for $z = 7.0$ and 7.3 LAEs have been conducted by Ota et al. (2010) and Shibuya et al. (2012), and these studies find that the number density and the Lyα luminosity density decrease from $z = 5.7$ to $7.0 - 7.3$. However, they cannot clearly find whether the Lyα LF evolves from $z = 6.6$ to $7.0 - 7.3$ due to the large uncertainties of their LF measurements. Their large uncertainties are originated from the relatively shallow imaging that just reaches the bright Lyα luminosity limit of $L(\mathrm{Ly}\alpha) \sim 10^{43}$ erg s^{-1}. The contradicted results of the Lyα LF evolution may be caused by small statistics and systematic uncertainties such as contamination and cosmic variance. To reliably investigate the evolution of the Lyα LF at $z \gtrsim 7$, one needs an ultra-deep narrowband imaging survey in large areas down to the Lyα luminosity limit comparable to those of $z \leq 6.6$ LAE samples.

Studies of the Lyα LF evolution are important for understanding galaxy evolution and cosmic reionization. The Lyα damping wing of neutral hydrogen in inter-galactic medium (IGM) around galaxies attenuates Lyα photons significantly. Thus, a volume-averaged neutral hydrogen fraction, x_{HI}, of IGM would be constrained by the evolution of the Lyα LF at the epoch of $x_{\mathrm{HI}} \sim 0.1 - 1.0$ (Malhotra & Rhoads 2004; Hu et al. 2005; Iye et al. 2006; Kashikawa et al. 2006, 2011; Ota et al. 2008, 2010; Ouchi et al. 2010; Shibuya et al. 2012). The evolution of the Lyα luminosity density between $z = 5.7$

konno@icrr.u-tokyo.ac.jp
[1] Institute for Cosmic Ray Research, The University of Tokyo, Kashiwa-no-ha, Kashiwa 277-8582, Japan
[2] Department of Astronomy, Graduate School of Science, The University of Tokyo, Hongo, Bunkyo-ku, Tokyo, 113-0033, Japan
[3] Kavli Institute for the Physics andMathematics of the Universe (Kavli IPMU), WPI, The University of Tokyo, Kashiwa, Chiba 277-8583, Japan
[4] Research Center for the Early Universe, Graduate School of Science, The University of Tokyo, Hongo, Bunkyo-ku, Tokyo, 113-0033, Japan
[5] Center for Computational Science, University of Tsukuba, Tsukuba, Ibaraki 305-8577, Japan
[6] National Astronomical Observatory of Japan, 2-21-1 Osawa, Mitaka, Tokyo 181-8588, Japan

and 6.6 suggests $x_{\rm HI} = 0.2 \pm 0.2$ at $z = 6.6$ that is corrected for the intrinsic UV luminosity evolution effect with the cosmic star formation rate density change (Ouchi et al. 2010). A Lyα emitting fraction of UV-continuum selected galaxies is similarly used for a probe of cosmic reionization. Previous studies report that the Lyα emitting fraction of Lyman break galaxies (LBGs) decreases from $z \sim 6$ to 7 in contrast to the increase of the Lyα emitting fraction from $z \sim 3$ to 6, and claim that the neutral hydrogen fraction increases from $z \sim 6$ to 7. (Pentericci et al. 2011; Schenker et al. 2012; Ono et al. 2012; Treu et al. 2012; Caruana et al. 2012, 2014; Pentericci et al. 2014; Schenker et al. 2014). By the comparison with theoretical models, these studies suggest $x_{\rm HI} \gtrsim 0.5$ at $z \sim 7$.

There are other observational studies to investigate when and how cosmic reionization took place. Observations of the Gunn & Peterson (1965) (GP) trough in quasar (QSO) spectra indicate $x_{\rm HI} \sim 10^{-4}$ at $z \sim 6$ (Fan et al. 2006), suggesting that cosmic reionization has been completed at this redshift. Measurements of the polarization of cosmic microwave background (CMB) by *WMAP* constraint the optical depth of Thomson scattering, $\tau_{\rm el} = 0.081 \pm 0.012$, and indicate that the universe would be reionized at $z_{\rm re}^{\rm inst} = 10.1 \pm 1.0$ for the case of instantaneous reionization (Hinshaw et al. 2013; Bennett et al. 2013). Recent observational studies with *Planck* show that the electron scattering optical depth is $\tau_{\rm el} = 0.089^{+0.012}_{-0.014}$, and that the instantaneous reionization redshift is $z_{\rm re}^{\rm inst} = 11.1 \pm 1.1$ (Planck Collaboration et al. 2013). Totani et al. (2006) estimate $x_{\rm HI}$ with the shape of Lyα damping wing absorption found in the optical afterglow spectrum of GRB 050904 at $z \sim 6.3$, and obtain $x_{\rm HI} < 0.17$ (68% confidence level) at this redshift. In the recent study with a GRB, the unprecedentedly bright optical afterglow spectrum of GRB 130606A at $z \sim 5.9$ suggests $x_{\rm HI} = 0.1 - 0.5$ (Totani et al. 2014). Mortlock et al. (2011) report observations of a QSO at $z = 7.085$, ULAS J1120+0641, and claim $x_{\rm HI} > 0.1$ at this redshift from the near-zone transmission profile. Bolton et al. (2011) use radiative transfer simulations with model absorptions of inhomogeneous IGM around ULAS J11201+0641, and obtain $x_{\rm HI} \gtrsim 0.1$.

Although the CMB observations rule out the instantaneous reionization at a late epoch, it is difficult to understand how the reionization proceeds in the cosmic history. As illustrated in Figure 23 of Ouchi et al. (2010), there are large uncertainties of the $x_{\rm HI}$ estimates from the previous observational studies, and one cannot distinguish between various models of reionization history. A redshift of ~ 7 is the observational limit of optical instruments that enable us to conduct a deep and wide-field imaging survey. The differences of reionization history in models are relatively large at $z \gtrsim 7$ (see Figure 23 of Ouchi et al. 2010). A measurement of the Lyα LF at $z \sim 7$ with a good statistical accuracy is useful to constrain $x_{\rm HI}$ near the observational limit and to address this issue of cosmic reionization history.

In this paper, we present the results of our ultra-deep narrowband imaging survey for $z = 7.3$ LAEs. Using this sample, we derive the Lyα LF with accuracies significantly better than those of previous $z \gtrsim 7$ studies. We investigate the Lyα LF evolution at $z \gtrsim 7$ with this Lyα LF, and discuss the cosmic reionization history. We describe the details of our $z = 7.3$ LAE survey and selection of our LAE candidates in Section 2. We derive the $z = 7.3$ Lyα LF and compare it with previous studies of $z \simeq 7.3$ in Section 3. We examine the evolution of the Lyα LF at $z = 5.7 - 7.3$, and discuss cosmic reionization with the constraints of the electron scattering optical depth measurements of CMB in Section 4. Throughout this paper, we adopt AB magnitudes (Oke 1974) and concordance cosmology with a parameter set of (h, $\Omega_{\rm m}$, Ω_Λ, σ_8) = (0.7, 0.3, 0.7, 0.8) consistent with the *WMAP* and *Planck* results (Hinshaw et al. 2013; Planck Collaboration et al. 2013).

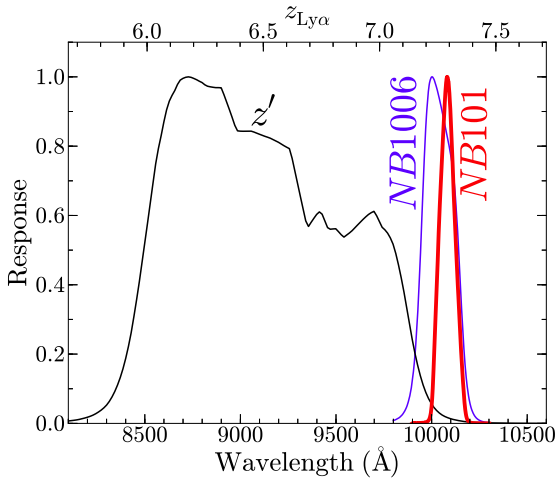

Figure 1. Filter response curve of *NB101* that is shown with the red line. The blue and black lines represent the response curves of *NB1006* and z' bands, respectively. These response curves are based on actual lab measurements, and include the quantum efficiency of Hamamatsu CCDs (Kamata et al. 2008), airmass, transmission+reflection of instrument, and telescope optics. For clarity, peaks of these curves are normalized to 1.0. The upper abscissa axis indicates a redshift of Lyα that corresponds to the wavelength. Note that *NB1006* widely covers a redshift range of $z = 7.2 - 7.3$, and that *NB101* targets a narrow redshift range centered at $z = 7.3$.

2. IMAGING OBSERVATIONS AND DATA REDUCTION

2.1. *NB101 Observations*

We have carried out an ultra-deep large-area narrowband imaging survey with Subaru/Suprime-Cam (Miyazaki et al. 2002) to study LAEs at $z = 7.3$ down to the faint Lyα luminosity limit. For these observations, we have developed a new custom narrowband filter, *NB101*. The filter transmission of *NB101* is centered at $\lambda_{\rm c} = 10095$Å and *NB101* is designed to have a narrow and sharp FWHM of $\Delta\lambda = 90$Å. The *NB101* filter identifies LAEs in the redshift range of $z = 7.302 \pm 0.037$. We show the filter response curve of our *NB101* in Figure 1. Note that there is a Suprime-Cam narrowband filter, *NB1006*, at a similar wavelength (Shibuya et al. 2012). The *NB1006* filter has a central wavelength of $\lambda_{\rm c} = 10052$Å slightly bluer than that of our *NB101* and an FWHM of $\Delta\lambda = 214$Å about 2-3 times broader than that of our *NB101*. Similarly, there is another Suprime-Cam narrowband filter of *NB973* targeting $z = 7.0$ LAEs with a central wavelength of $\lambda_{\rm c} = 9755$Å and an FWHM of $\Delta\lambda \sim 200$Å (Iye et al. 2006; Ota et al. 2008, 2010) that is also much broader than the FWHM of our *NB101* filter. Since our *NB101* filter has a significantly narrower/shaper FWHM than the *NB1006* and *NB973* filters, our *NB101* filter is more sensitive to an emission line than the *NB1006* and *NB973* filters. Although the survey volume is smaller for *NB101* than for *NB1006* and *NB973*, the line sensitivity is more important for the observational studies of

Table 1
Summary of Our Observations and Data

Field	Band	Exposure Time (s)	PSF size[a] (arcsec)	Area (arcmin^2)	$m_{\rm lim}$[b] (5σ AB mag)	Date of Observations
SXDS	*NB101*	57600	0.78		24.6	2010 Dec 29−2011 Jan 1
	NB101	73200	0.86		24.3	2012 Dec 11−14
	NB101 (Final)	130800[c]	0.80	7.9×10^2	24.9	—
COSMOS	*NB101*	83510.6	0.72		24.8	2010 Dec 29−2011 Jan 2
	NB101	61200	0.99		23.7	2012 Dec 11−14
	NB101	105600	0.90		24.4	2013 Feb 9−12
	NB101 (Final)	250310.6[c]	0.77	8.4×10^2	25.1	—
Archival Broadband Data[d]						
SXDS	*B*		0.84	7.9×10^2	28.1	
	V		0.84		27.7	
	R		0.84		27.6	
	i'		0.84		27.3	
	z'		0.80		26.9	
COSMOS	*B*		0.95	8.4×10^2	27.7	
	V		1.32		26.4	
	R		1.05		26.9	
	i'		0.95		26.6	
	z'		0.84		26.8	

[a] The FWHM value of PSF.
[b] The 5σ limiting magnitude in a circular aperture with a diameter of $2\times$ PSF FWHM.
[c] The total on-source integration times correspond to 36.3 and 69.5 hours in the SXDS and COSMOS fields, respectively.
[d] The Broadband images are archival data presented in Furusawa et al. (2008) for SXDS and Capak et al. (2007) for COSMOS. The SXDS and COSMOS z' data include the images taken by the Subaru intensive program conducted in $2009 - 2011$ (PI: H. Furusawa).

$z \gtrsim 7$ sources whose LF's exponential edge is near the observational limit. At $z = 7.3$, our *NB101* filter allows us to reach a Lyα flux limit faster than the previous Shibuya et al.'s *NB1006* surveys by $\sim 160\%$. Thus, we can reach the Lyα luminosity limit of LAEs much fainter than the previous Subaru studies for $z \sim 7$ LAEs.

With our new *NB101* filter, we observed two independent fields, Subaru/*XMM-Newton* Deep Survey (SXDS) and Cosmic Evolution Survey (COSMOS) fields. The SXDS field is located at $02^{\rm h}18^{\rm m}00^{\rm s}.0$, $-05^{\rm d}00'00''$ (J2000) (Furusawa et al. 2008; Ouchi et al. 2008, 2010), It consists of five subfields of ~ 0.2 deg^2, SXDS-C, N, S, E and W. We choose a field of ~ 0.2 deg^2 to cover the southern half of SXDS-C and the northern half of SXDS-S, where bright stars do not exist and *HST* CANDELS (Grogin et al. 2011; Koekemoer et al. 2011), *UKIRT* UKIDSS (Lawrence et al. 2007), *Spitzer* SpUDS (PI: J. Dunlop), and SEDS (PI: G. Fazio) data are also available (see Figure 2 in Ota et al. 2010). The target field of COSMOS is an area of ~ 0.2 deg^2 centered at $10^{\rm h}00^{\rm m}28^{\rm s}.6$, $+02^{\rm d}12'21''.0$ (J2000) (Scoville et al. 2007). In the COSMOS field, there exist CANDELS and UltraVISTA (PI: J. Dunlop) imaging data. Each of SXDS and COSMOS field is covered by one pointing of Suprime-Cam whose field of view is 918 arcmin^2. Our observations were conducted in $2010 - 2013$. The total on-source integration time is 106 hours where 36.3 and 69.5-hour data were obtained in the SXDS and COSMOS fields, respectively. We summarize the details of our observations as well as image qualities in Table 1. In addition to these *NB101* images, we use archival data of deep broadband (*B*, *V*, *R*, i' and z') images of the SXDS and COSMOS projects (Furusawa et al. 2008 and Capak et al. 2007 for SXDS and COSMOS fields, respectively). The properties of these broadband-data are also listed in Table 1.

Our *NB101* data are reduced with the Suprime-Cam Deep field REDuction package (SDFRED; Yagi et al. 2002; Ouchi et al. 2004). In this reduction process, we perform bias subtraction, flat-fielding, distortion+atmospheric-dispersion correction, sky subtraction, image alignments, and stacking. Before the image alignments, we mask out areas contaminated by spurious signals and meteor+satellite trails. We remove cosmic rays with a rejected-mean algorithm. We make composite images from each one-night data set. Then, we stack all of these one-night composite images with weights based on signal-to-noise ratios of these images to make the final images. To obtain the weights, we measure the photometric-zero point and the limiting magnitude for each one-night composite image. For measuring colors of objects precisely, we align the reduced *NB101* images with the broadband images based on hundreds of bright stellar objects commonly detected in the *NB101* and broadband images. We calculate the photometric-zero points from our standard star data. Estimating the photometric-zero points, we took data of spectrophotometric standard stars of G191-B2B and GD153 (Bohlin et al. 1995) with *NB101*. We check these photometric-zero points with stellar sequences of observed stellar objects in our fields and 175 Galactic stars of Gunn & Stryker (1983) on a two-color diagram of $z' - NB101$ vs. $i' - z'$. After the check of the photometric-zero points, we estimate the limiting magnitudes of our images.

The final *NB101* images of SXDS and COSMOS have the seeing size of $\simeq 0.''8$, and reach the 5σ magnitude of $\simeq 25.0$ mag. We summarize the qualities of our final *NB101* images in Table 1. We use pixels of the imaging data neither contaminated with halos of bright stars, CCD blooming, nor low signal-to-noise ratio region near the edge of Suprime-Cam field of view. These low-quality regions are masked out, and the effective survey areas are 7.9×10^2 and 8.4×10^2 arcmin^2

in the SXDS and COSMOS fields, respectively. Thus, our total survey area is 1.6×10^3 arcmin^2, i.e. $\simeq 0.5$ deg^2. If we assume a simple top-hat selection function for LAEs whose redshift distribution is defined by the FWHM of *NB101*, these effective survey areas correspond to the comoving survey volumes of 1.2×10^5 and 1.3×10^5 Mpc^3 for the SXDS and COSMOS fields, respectively.

2.2. *Photometry*

The source detection and photometry are performed with SExtractor version 2.5.0 (Bertin & Arnouts 1996). Sources are identified with the criterion: contiguous > 5 pixels with a flux greater than the 2σ level of sky fluctuation. We conduct the source detection in our *NB101* images, and obtain the broadband photometry at the positions of the sources. We detect a total of 69,387 objects in the SXDS and COSMOS fields down to the 5σ limits of aperture magnitudes that are *NB101* $= 24.9$ (SXDS) and 25.1 (COSMOS). Here, we define the aperture magnitude of MAG_APER of SExtractor with an aperture size of $2\times$ PSF FWHM, and use the aperture magnitude for measuring colors of objects. For total magnitude estimates, we apply an aperture correction value of 0.3 to the aperture magnitudes. Because MAG_AUTO of SExtractor gives biased magnitude measurements for faint objects around the detection limits, we use this aperture correction technique. Ono et al. (2012) study z-dropout galaxies at $z \sim 7$ using Subaru/Suprime-Cam data, and derive the aperture correction value of ~ 0.3 mag. We apply the same aperture correction value as Ono et al. (2012) because the PSF FWHM of the Ono et al's data ($\sim 0.''8 - 0.''9$) is similar to that of our NB101 data. The reliability of this technique is investigated in Section 2.3.

2.3. *Photometric Sample of $z = 7.3$ LAEs*

We isolate $z = 7.3$ LAE candidates from all of the objects detected in Section 2.2 based on a narrowband excess of Lyα emission and no detection of blue continuum flux. Figures 2 and 3 show the color-magnitude diagrams of the *NB101* magnitude and the narrowband excess color, $z' -$ *NB101*, for the objects detected in SXDS and COSMOS fields. The detected objects have a color of $z' -$ *NB101* $\simeq +0.2$ on average in the magnitude range of $22 <$ *NB101* < 24. To determine the $z' -$ *NB101* color criterion for our LAE candidate selection, we assume a model spectrum of $z = 7.3$ LAE that has a Lyα line and a flat ultraviolet (UV) continuum (i.e., $f_\nu = $ const.) with an IGM absorption (Madau 1995). Based on the model spectrum, we adopt the criterion that $z' -$ *NB101* $\geqslant 3.0$, which corresponds to LAEs with the rest-frame equivalent width, EW$_0$, of EW$_0 \gtrsim 0$Å, which is similar to the criterion adopted by Shibuya et al. (2012). Note that this small limit of the EW$_0$ criterion gives a chance to select high-z dropout galaxies and foreground red objects, due to photometric errors, which are the potential contamination sources. Because this EW$_0$ limit gives a more complete sample, we apply this EW$_0$ limit. We discuss the effect of this small EW$_0$ limit in Section 4.2.

Adding other criterion of no detectable continuum flux bluer than Lyα, we define the selection criteria of $z = 7.3$ LAEs:

$$\begin{aligned} &\textit{NB101} < \textit{NB101}_{5\sigma} \text{ and } B > B_{3\sigma} \\ &\text{and } V > V_{3\sigma} \text{ and } R > R_{3\sigma} \text{ and } i' > i'_{3\sigma} \\ &\text{and } [(z' - \textit{NB101} \geqslant 3.0) \text{ or } (z' > z'_{3\sigma})] , \end{aligned} \tag{1}$$

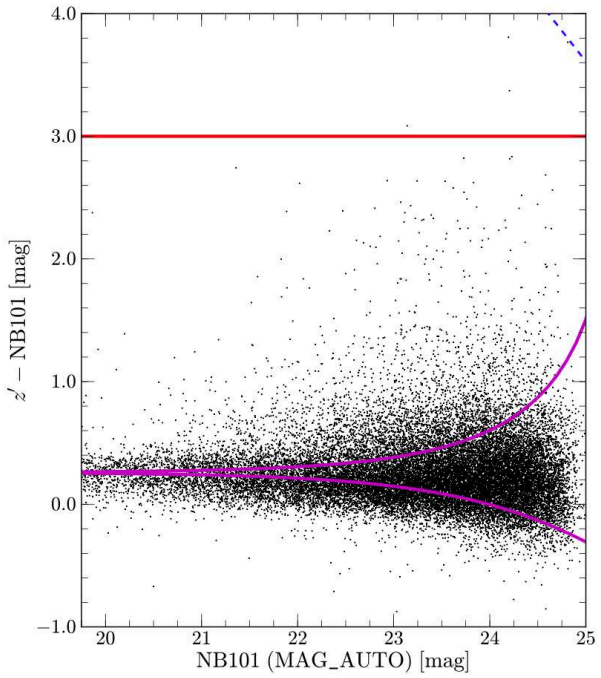

Figure 2. Color-magnitude diagram of $z' -$ *NB101* vs. *NB101* for objects detected in the SXDS field. The black dots show all of the detected objects. The blue-dashed and magenta-solid lines indicate the 1σ limit of the z' magnitude and the 3σ error of the $z' -$ *NB101* color, respectively. The red line represents the $z' -$ *NB101* color criterion for the selection of our $z = 7.3$ LAEs.

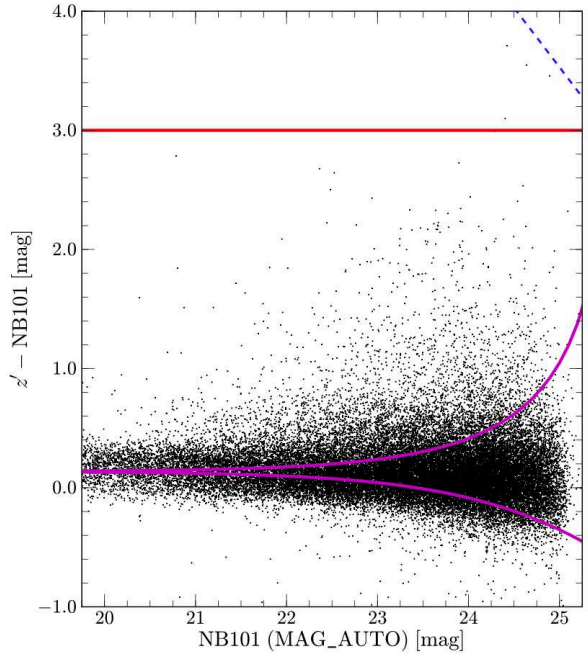

Figure 3. Same as Figure 2, but for the COSMOS field.

where the indices of 5σ and 3σ denote the 5σ and 3σ detection limits of the images, respectively.

We apply these photometric criteria to all of our detected objects, and identify three and four $z = 7.3$ LAE candidates in the SXDS and COSMOS fields, respectively. We show the snapshot images of these LAE candidates in Figure 4. In our *NB101* ultra-deep survey, we have reached a 5σ limiting flux

of $\simeq 6.5\times10^{-18}$ erg s^{-1} cm^{-2} corresponding to a limiting luminosity of $L_{\rm Ly\alpha} \simeq 4.1\times10^{42}$ erg s^{-1} in the SXDS field, and $\simeq 3.8\times10^{-18}$ erg s^{-1} cm^{-2} equivalent to $L_{\rm Ly\alpha} \simeq 2.4\times10^{42}$ erg s^{-1} in the COSMOS field. These limiting luminosities are derived from the 5σ limiting magnitudes of *NB101* and the 1σ limiting magnitudes of z'. These are conservative estimates, because the limiting luminosity values are larger than those calculated with the $> 1\sigma$ limiting magnitudes of z'. In the calculations for the Lyα luminosities, we assume that Lyα emission is placed at the central wavelength of the narrow band. Ouchi et al. (2008) derive the Lyα luminosities in the same manner as ours, and compare these Lyα luminosities with spectroscopic luminosities. They find that both measurements agree well within the error bars, and that the difference of these values is small (see Section 3.3 for the effects of the Lyα luminosity uncertainties in Lyα LF derivation). The *NB101* image of COSMOS field is the deepest image in our *NB101* data. The 5σ limiting luminosity in the COSMOS field is about 4 times deeper than previous Subaru studies for LAEs at $z \sim 7$ (Ota et al. 2008, 2010; Shibuya et al. 2012). Moreover, the 5σ limiting luminosity is comparable with those of previous Subaru $z = 3.1-6.6$ LAE surveys (Shimasaku et al. 2006; Kashikawa et al. 2006, 2011; Ouchi et al. 2008, 2010).

We present the photometric properties of our $z = 7.3$ LAE candidates in Table 2. The total magnitudes listed in Table 2 are obtained by the aperture-correction technique explained in Section 2.2. We compare the total magnitude and MAG_AUTO of SExtractor for the most luminous LAE candidate that probably includes a negligible bias in the MAG_AUTO estimate, and find that these two magnitudes are consistent within the errors. Thus, it is reasonable to use the total magnitudes given by the aperture-correction technique that requires the assumption that $z = 7.3$ LAEs are point sources (Ono et al. 2010, 2012).

We investigate our $z = 7.3$ LAE candidates in the *J* and *H* images of *HST* CANDELS fields that are subfields of our COSMOS and SXDS survey areas. Two out of seven LAE candidates, NB101-COSMOS-37050 and NB101-COSMOS-37548, fall in the CANDELS field of COSMOS. We detect NB101-COSMOS-37050 both in the *J* and *H* images (Figure 4), but NB101-COSMOS-37548 neither in the *J* nor *H* data. We obtain the *J* and *H* magnitudes of NB101-COSMOS-37050, and present the magnitudes in Table 2. There are no counterparts of LAE candidates found in the CANDELS field of SXDS.

We examine whether $z = 7.2-7.3$ LAEs found by Shibuya et al. (2012) are identified in our *NB101* data. Shibuya et al. (2012) have observed the SXDS subfield same as our survey area with their *NB1006* filter (Section 2.1), and obtained two photometric LAE candidates, SXDS-NB1006-1 and SXDS-NB1006-2. However, both of two LAEs of Shibuya et al. (2012) are not detected in our *NB101* images. Because Shibuya et al. (2012) report that their spectroscopy indicates that one of them, SXDS-NB1006-2, resides at $z = 7.215$, the redshift of SXDS-NB1006-2 is out of our survey redshift range of $z = 7.302 \pm 0.037$ where *NB101* has a sensitivity for a Lyα emission line. Thus, the reason for no detection of SXDS-NB1006-2 is clear, while the reason for another object, SXDS-NB1006-1, is unknown. Since SXDS-NB1006-1 is not confirmed by their spectroscopic follow-up observations, it is possible that the Lyα emission of SXDS-NB1006-1 also falls in the wavelength where *NB101* does not cover. Note that the FWHM of *NB1006* is 214Å, while *NB101* is only 90Å (Section 2.1).

3. LUMINOSITY FUNCTION

3.1. *Contamination of Our Sample*

We investigate the contamination of our $z = 7.3$ LAE sample. The sources of possible contamination are spurious objects, transients, and foreground interlopers. First, our *NB101* images of SXDS and COSMOS fields are taken in 2010−2012 and 2010−2013, respectively (see Table 1). We stack *NB101* data of SXDS field observed in 2010−2011 and 2012, and obtain *NB101* images for the two epochs. Similarly, we make three *NB101* stacked images of COSMOS field at three epochs, 2010−2011, 2012, and 2013. The 5σ limiting magnitudes of these epoch images are summarized in Table 1. The results of independent photometry at the different epochs of our observations are shown in Table 3. All of the magnitudes of our LAE candidates in the multi-epochs are consistent within the $\simeq 95\%$-significance levels of the photometric errors. We find no variable signatures of transients in our LAEs. Because our LAEs are selected from narrowband images taken over 3-4 years, a fraction of transient contamination in our LAE sample is very small. Similarly, all of our LAEs, except NB101-SXDS-46782 and NB101-COSMOS-37050, are detected at the > 3 sigma levels in the ≥ 2 epoch images. Thus, our LAEs, except NB101-SXDS-46782 and NB101-COSMOS-37050, are not spurious sources. NB101-SXDS-46782 and NB101-COSMOS-37050 are found only at the $\simeq 2\sigma$ levels in the 2012 and 2012-2013 epoch images, respectively. However, we have identified the sources of NB101-SXDS-46782 and NB101-COSMOS-37050 in these epoch images by visual inspection. It is likely that NB101-SXDS-46782 and NB101-COSMOS-37050 are also not spurious sources. Second, spectroscopic follow-up observations for one of our candidates, NB101-SXDS-2904, were conducted with Keck/NIRSPEC, LRIS and MOSFIRE, and a single emission line that is probably Lyα is clearly detected from this object by all of these Keck spectroscopic observations (M. Ouchi et al. in preperation). Although only one LAE in our sample is observed by spectroscopy, no foreground interlopers are, so far, found by spectroscopic observations.

3.2. *Detection Completeness and Surface Number Density*

We estimate detection completeness as a function of the *NB101* magnitude by Monte-Carlo simulations. We distribute a number of pseudo LAEs with various magnitudes in our *NB101* images, and detect the pseudo LAEs in the same manner as our source extraction for real sources (Section 2.2). Here, we assume that $z = 7.3$ LAEs are point sources whose profiles are obtained by the stack of bright point sources in our *NB101* images. We define the detection completeness as the fraction of the numbers of the extracted pseudo LAEs to all of the input pseudo LAEs, and obtain the detection completeness presented in Figure 5. We find that the detection completeness is typically $\gtrsim 90\%$ for luminous sources with *NB101* $\lesssim 24.5$ and nearly 50% at around the 5σ limiting magnitude of *NB101* $\simeq 25$.

Figure 6 shows the surface number densities of $z = 7.3$ LAEs. The surface number densities are calculated by dividing the number counts of LAEs by our effective survey areas shown in Section 2.1. We correct these surface number densities for the detection completeness. The uncertainties of the surface densities of $z = 7.3$ LAEs are defined with the Poisson errors for small number statistics (Gehrels 1986). The val-

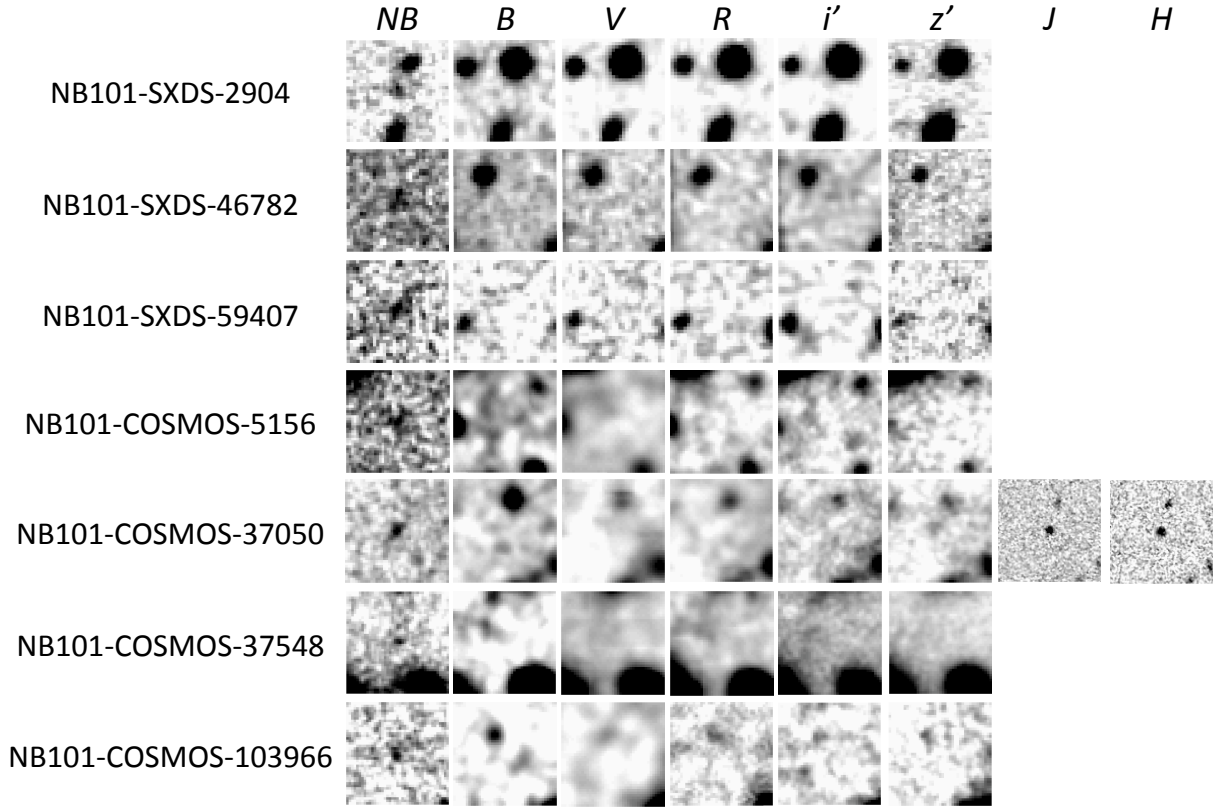

Figure 4. Snapshots of our $z = 7.3$ LAE candidates. The size of each image is $6'' \times 6''$. North is up and east is to the left.

Table 2
Our $z = 7.3$ LAE Candidates

ID	B	V	R	i'	z'	*NB101*[a]	*NB101*(total)[b]	J[a]	H[a]	$L(\mathrm{Ly}\alpha)$ (10^{42} erg s^{-1})
NB101-SXDS-2904	> 28.6	> 28.3	> 28.1	> 27.8	> 27.4	$24.50^{+0.16}_{-0.14}$	$24.20^{+0.12}_{-0.11}$	—	—	9.68
NB101-SXDS-46782	> 28.6	> 28.3	> 28.1	> 27.8	> 27.4	$24.84^{+0.23}_{-0.19}$	$24.54^{+0.17}_{-0.15}$	—	—	5.72
NB101-SXDS-59407	> 28.6	> 28.3	> 28.1	> 27.8	> 27.4	$24.80^{+0.22}_{-0.18}$	$24.50^{+0.16}_{-0.14}$	—	—	6.13
NB101-COSMOS-5156	> 28.3	> 27.0	> 27.4	> 27.2	> 27.3	$24.98^{+0.21}_{-0.18}$	$24.68^{+0.16}_{-0.14}$	—	—	3.82
NB101-COSMOS-37050	> 28.3	> 27.0	> 27.4	> 27.2	> 27.3	$24.84^{+0.19}_{-0.16}$	$24.54^{+0.14}_{-0.12}$	$25.42^{+0.05}_{-0.05}$	$25.39^{+0.06}_{-0.05}$	5.11
NB101-COSMOS-37548	> 28.3	> 27.0	> 27.4	> 27.2	> 27.3	$25.03^{+0.23}_{-0.19}$	$24.73^{+0.17}_{-0.14}$	—	—	3.39
NB101-COSMOS-103966	> 28.3	> 27.0	> 27.4	> 27.2	> 27.3	$25.07^{+0.23}_{-0.19}$	$24.77^{+0.17}_{-0.15}$	—	—	3.01

[a] The magnitudes with the 1σ error measured with an aperture whose diameter is $2\times$ PSF FWHM.
[b] The total magnitudes which are obtained by the aperture-correction technique explained in Section 2.2

ues of columns "0.8413" in Tables 1 and 2 of Gehrels (1986) are used for the upper and lower limits of the Poisson errors, respectively.

3.3. $z = 7.3$ Lyα Luminosity Function

We calculate the Lyα EW$_0$ of LAEs from the *NB101* and z' magnitudes, and estimate the Lyα luminosities of LAEs with these EW$_0$ and the *NB101* total magnitudes. For the errors of the Lyα luminosities, we carry out Monte Carlo simulations under the assumption that the spectrum of LAEs has a Lyα line and a flat UV continuum (i.e., $f_\nu = $ const.) with the IGM absorption, following the methods applied in Shimasaku et al. (2006); Ouchi et al. (2008, 2010). Again, in the calculations for the Lyα luminosities, we assume that Lyα emission is placed at the central wavelength of the narrow band. Similarly, we derive the Lyα LF of $z = 7.3$ LAEs in the same manner as Ouchi et al. (2008, 2010). We calculate the volume number densities of LAEs in each Lyα luminosity bin, dividing the observed surface number densities of LAEs by our survey volumes based on a top-hat filter transmission curve assumption. This procedure of Lyα LF derivation is known as the classical method. Note that there are two uncertainties of the Lyα LFs derived by the classical method. (1) A Lyα flux of a LAE at the fixed narrowband magnitude varies by the LAE's redshift. (2) A redshift distribution of LAEs depends on a Lyα EW. In order to evaluate such uncertainties, Shimasaku et al. (2006) and Ouchi et al. (2008) perform Monte Carlo simulations. In these simulations, they generate a mock catalogue of LAEs with a set of Schechter parameters (ϕ^*, L^*, α) and a Gaussian sigma for a probability distribu-

Table 3
Magnitudes of our $z = 7.3$ LAE Candidates in the Different Epoch

ID	*NB101*[a] (2010)[b]	*NB101*[a] (2012)[b]	*NB101*[a] (2013)[b]
NB101-SXDS-2904	$24.51^{+0.22}_{-0.18}$	$24.38^{+0.26}_{-0.21}$	—
NB101-SXDS-46782	$24.74^{+0.28}_{-0.22}$	$25.03^{+0.54}_{-0.36}$	—
NB101-SXDS-59407	$24.79^{+0.30}_{-0.23}$	$24.76^{+0.40}_{-0.29}$	—
NB101-COSMOS-5156	$25.03^{+0.31}_{-0.24}$	$24.65^{+0.71}_{-0.43}$	$24.86^{+0.40}_{-0.29}$
NB101-COSMOS-37050	$24.64^{+0.21}_{-0.17}$	$24.69^{+0.75}_{-0.44}$	$25.48^{+0.84}_{-0.47}$
NB101-COSMOS-37548	$25.19^{+0.37}_{-0.27}$	$24.07^{+0.36}_{-0.27}$	$24.92^{+0.42}_{-0.30}$
NB101-COSMOS-103966	$25.11^{+0.34}_{-0.26}$	$24.92^{+1.04}_{-0.52}$	$24.76^{+0.35}_{-0.27}$

[a] The magnitudes with the 1σ error measured with an aperture whose diameter is $2\times$ PSF FWHM.
[b] The values in parenthesis present the epochs of data used for the stacked images. 2010, 2012, and 2013 indicate the epochs of 2010 − 2011, 2012, and 2013 observing periods, respectively.

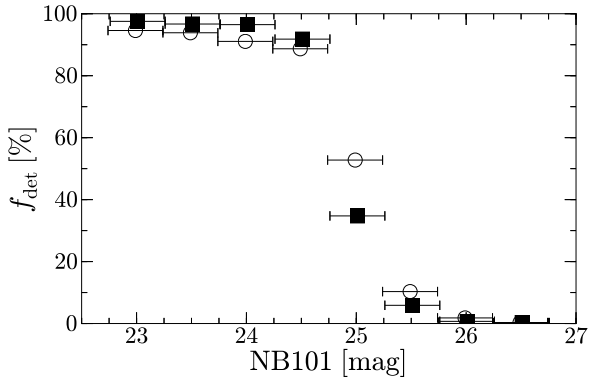

Figure 5. Detection completeness of our *NB101* images. The filled squares and open circles represent the completeness in the SXDS and COSMOS fields, respectively.

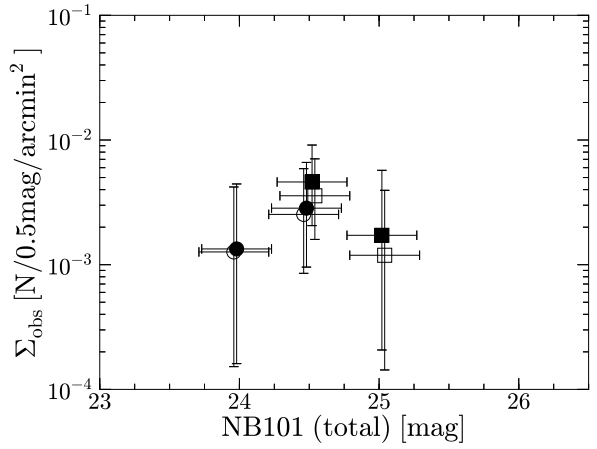

Figure 6. Surface number density of our $z = 7.3$ LAEs as a function of the *NB101* magnitude. The circles and squares represent the surface number densities in the SXDS and COSMOS fields. The filled and open symbols indicate the ones with and without the detection completeness correction, respectively.

tion of Lyα EW$_0$, and uniformly distribute the LAEs of the mock catalog in a comoving volume over the redshift range that a narrowband covers. They "observe" these LAEs with the narrow and broad bands to be the same as the real band response. They select LAEs using the same criteria as was used for selecting the actual LAEs and derive the number densities and color distributions from the mock catalog. By comparing the results of these simulations with the observational results, they find the best-fit Schechter parameters of Lyα LFs (see Shimasaku et al. 2006; Ouchi et al. 2008, for more details of the simulations). They confirm that the LFs estimated from the simulations are consistent with those derived by the classical method.

Figure 7 presents the Lyα LF of our $z = 7.3$ LAEs in the entire fields that include both the SXDS and COSMOS fields. The error bars of this LF include uncertainties from Poisson statistics and cosmic variance. Here, we estimate the cosmic variance uncertainty, $\sigma_{\rm g}$, with

$$\sigma_{\rm g} = b_{\rm g}\sigma_{\rm DM}(z, R), \quad (2)$$

where $b_{\rm g}$ and $\sigma_{\rm DM}(z, R)$ are the bias parameter and the density fluctuation of dark matter at a redshift of z in a radius of R, respectively. We calculate $\sigma_{\rm DM}(z, R)$ with the growth factor, following Carroll et al. (1992) with the transfer function given by Bardeen et al. (1986) (see also Mo & White 2002). Note that the radius of $\sigma_{\rm DM}(z, R)$ corresponds to that of a sphere which has the survey volume same as ours, i.e. 2.5×10^5 Mpc^3. The value of $\sigma_{\rm DM}(z, R)$ at $z = 7.3$ is estimated to be 0.041. Because the bias parameter of $b_{\rm g} = 3.6 \pm 0.7$ is obtained for $z = 6.6$ LAEs (Ouchi et al. 2010), we adopt $b_{\rm g} \simeq 4$ for $z = 7.3$ LAEs under the assumption that $b_{\rm g}$ does not significantly evolve at $z = 6.6-7.3$. With this procedure, we estimate the cosmic variance uncertainty to be $\sigma_{\rm g} \simeq 0.16$. In Figure 7, we plot the LFs from two independent fields of SXDS and COSMOS. Because these LFs are consistent within the statistical+cosmic variance uncertainties of the entire-field LF in two luminosity bins, $\log L_{{\rm Ly}\alpha} = 42.7$ and 42.9 erg s^{-1}, we confirm that our errors of the entire-field LF explain the cosmic variance effects based on the real observational data of SXDS and COSMOS on the independent sky.

We fit a Shechter function (Schechter 1976) to our $z = 7.3$ Lyα LF by minimum χ^2 fitting. The Shechter function is defined by

$$\phi(L)dL = \phi^*(L/L^*)^\alpha \exp(-L/L^*)d(L/L^*), \quad (3)$$

where ϕ^* and L^* represent the characteristic number density and luminosity, respectively, and α is a power-law slope

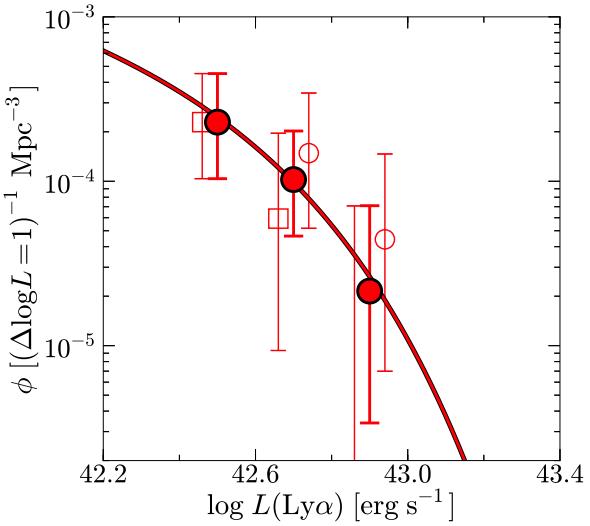

Figure 7. Lyα LF of our $z = 7.3$ LAEs. The red filled circles represent the Lyα LF derived with the data of the entire fields, i.e. both the SXDS and COSMOS fields. The red open circles and squares denote our Lyα LFs estimated with the data of the SXDS and COSMOS fields, respectively. In the brightest luminosity bin, we also plot the upper error of the Lyα LF in COSMOS field. The best-fit Schechter function for the Lyα LF of the entire fields is shown with the red curve.

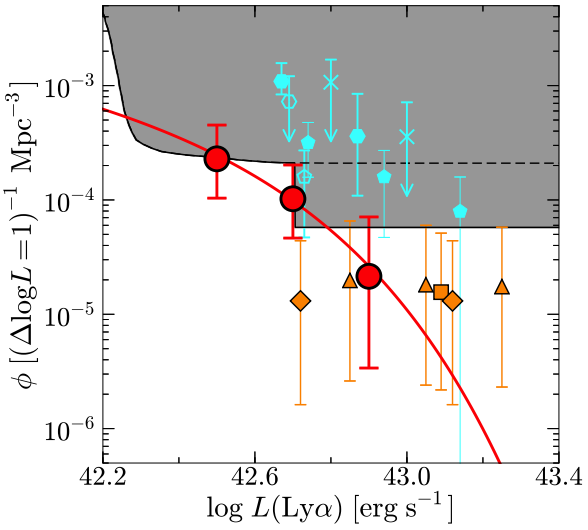

Figure 8. Comparison of our $z = 7.3$ Lyα LF with the previous measurements of Lyα LF at $z = 7.3 \pm 0.4$. The red circles denote our $z = 7.3$ Lyα LF, and the red curve is the best-fit Schechter function. The orange diamonds, square, and triangles represent the Subaru measurements of the Lyα LF at $z = 7.0 - 7.3$ given by Shibuya et al. (2012), Iye et al. (2006), and Ota et al. (2010), respectively. The gray region indicates the parameter space of $z = 7.7$ Lyα LF ruled out by the VLT observations (Clément et al. 2012). The black dashed line is the upper limit of the number density determined by the VLT photometric observations, while the black solid line represents the upper limits from the combination of the VLT photometric and spectroscopic data (Clément et al. 2012). The cyan filled pentagons, hexagons, and crosses denote the 4m-telescope estimates of the Lyα LF at $z = 7.7$ obtained by Hibon et al. (2010), Krug et al. (2012), and Tilvi et al. (2010), respectively. The cyan open pentagons and hexagons are the same as the cyan filled pentagons and hexagons, but for the results of no emission-line detection of the spectroscopic follow-up observations for the 4m-telescope samples, which are presented in Clément et al. (2012) and Faisst et al. (2014), respectively.

of the faint-end LF. Because the luminosity range of our LF is not wide, the parameter of α in the Schechter function cannot be determined. We fix a power-law slope of $\alpha = -1.5$, which is a fiducial value used for low-z Lyα LFs (e.g., Malhotra & Rhoads 2004; Kashikawa et al. 2006, 2011; Ouchi et al. 2008, 2010). In the calculations for the χ^2 values, we adopt an upper error as 1σ in the case that models are beyond the data point of our LF. Similarly, a lower error is adopted in the case that models are below the data point of our LF. We obtain the best-fit Schechter parameters of $\phi^* = 3.7^{+17.6}_{-3.3} \times 10^{-4}\ \mathrm{Mpc}^3$ and $L^*_{\mathrm{Ly}\alpha} = 2.7^{+8.0}_{-1.2} \times 10^{42}\ \mathrm{erg\ s}^{-1}$ with the fixed $\alpha = -1.5$, and present these best-fit values in Table 4. The best-fit Schechter function is shown in Figure 7 with the red solid line.

3.4. *Comparison with $z \simeq 7.3$ Lyα LFs of Previous Studies*

We compare our $z = 7.3$ Lyα LF with those obtained by previous studies for LAEs at $z = 7.0 - 7.7$, assuming that the Lyα LF does not significantly evolve at $z = 7.3 \pm 0.4$. In Figure 8, we plot the previous Subaru measurements of the Lyα LF at $z = 7.0$ (Iye et al. 2006; Ota et al. 2008, 2010) and 7.3 (Shibuya et al. 2012) that include spectroscopy results. These previous Subaru results are consistent with the bright-end of our Lyα LF within the uncertainties, while these previous Subaru studies typically reach $L(\mathrm{Ly}\alpha) \sim 10^{43}$ erg s^{-1} that is significantly shallower than our ultra-deep survey. Similarly, the black solid line of Figure 8 presents the upper limits of the Lyα LF given by the VLT observations that identify no LAEs at $z = 7.7$ (Clément et al. 2012). These upper limits of the Lyα LF are consistent with our results.

On the other hand, we find discrepancies between these Subaru+VLT results including ours and the previous 4m-telescope results of $z = 7.7$ LAEs that are reported by Hibon et al. (2010), Tilvi et al. (2010), and Krug et al. (2012). In Figure 8, the number densities of the Lyα LF of the 4m-telescope results are about a factor of several or an order of magnitude larger than those of the Subaru+VLT results beyond the uncertainties. We discuss these discrepancies of $z \simeq 7.3$ Lyα LF measurements between the Subaru+VLT and 4m-telescope results in Section 4.1.

4. DISCUSSION

4.1. *Discrepancies of $z \simeq 7.3$ Lyα LF Estimates*

In Section 3.4, we find the discrepancies of $z \simeq 7.3$ Lyα LFs between the Subaru+VLT results (including ours) and the 4m-telescope results (Hibon et al. 2010; Tilvi et al. 2010; Krug et al. 2012). There is a possibility to explain the discrepancies by the cosmic variance effects. However, all of these 4m-telescope LF measurements fall above the Subaru+VLT LF estimates. It is difficult to reconcile all of the 4m-telescope measurements by the chance fluctuations of cosmic variance. Another possibility is contamination. Clément et al. (2012) mention the results of the VLT/X-Shooter spectroscopic follow-up observations for the brightest five out of seven photometric LAE candidates of Hibon et al. (2010), and report that no Lyα emission lines from these Hibon et al.'s candidates are identified (see J. G. Cuby et al. in preparation). More recently, Faisst et al. (2014) conduct the spectroscopic follow-up observations for the brightest two out of four photometric candidates of Krug et al. (2012), and they detect no Lyα emission line from the Krug et al.'s candidates (see also Jiang et al. 2013). There is a similar spectroscopic study that reports no detection of Lyα from $z > 7$ LAEs whose sample is made with 4m-telescope data (Matthee et al. 2014). Thus, the photometric samples of Hibon et al. (2010) and Krug et al. (2012) include a significant number of contamination sources

that are probably more than a half of their LAE candidates, which are indicated by the spectroscopic follow-up studies. Spectroscopic observations for the LAE candidates of Tilvi et al. (2010) have not been carried out so far. However, it is possible that the Tilvi et al.'s sample includes a large number of contamination, because of the sample selection from the 4m-telescope data similar to those of Hibon et al. (2010) and Krug et al. (2012). We conclude that our Lyα LF is consistent with those from the Subaru and VLT studies whose results are supported by the spectroscopic observations (Iye et al. 2006; Ota et al. 2008, 2010; Shibuya et al. 2012; Clément et al. 2012), and that our Lyα LF agrees with the results of the recent deep spectroscopic follow-up observations for the LAE candidates from the 4m-telescope data (Clément et al. 2012; Faisst et al. 2014; Jiang et al. 2013).

4.2. *Decrease of Lyα LF from $z = 6.6$ to 7.3*

In this section, we examine whether the Lyα LF evolves from $z = 6.6$ to 7.3. As described in Section 2.3, we reach the Lyα limiting luminosity of 2.4×10^{42} erg s^{-1} that is comparable with those of previous Subaru $z = 3.1 - 6.6$ studies (Shimasaku et al. 2006; Kashikawa et al. 2006, 2011; Ouchi et al. 2008, 2010; Hu et al. 2010). Moreover, the size of survey area, $\simeq 0.5$ deg^2, is comparable with these Subaru studies. Our ultra-deep observations in the large areas allow us to perform a fair comparison of the Lyα LFs at different redshifts. We compare our Lyα LF at $z = 7.3$ with those at $z = 5.7$ and 6.6 in Figure 9, and summarize the best-fit Schechter parameters at $z = 5.7$, 6.6, and 7.3 in Table 4. For the $z = 5.7$ and 6.6 data, we use the Lyα LF measurements of Ouchi et al. (2010) derived from the largest LAE samples, to date, at these redshifts, and the Lyα LF measurements include all of the major Subaru survey data (Shimasaku et al. 2006; Kashikawa et al. 2006, 2011) and the cosmic variance uncertainties in their errors. Nevertheless, the difference of the best-estimate Lyα LFs is negligibly small between these studies. In Figure 9, we find a significant decrease of the Lyα LFs from $z = 6.6$ to 7.3 largely beyond the error bars. In our survey, we expect to find 65 $z = 7.3$ LAEs in the case of no Lyα LF evolution from $z = 6.6$ to 7.3, but identify only 7 $z = 7.3$ LAEs by our observations that are about an order of magnitude smaller than the expected LAEs.

To quantify this evolution, we evaluate the error distribution of Schechter parameters. Because we fix the Schechter parameter of α to -1.5, we examine the error distribution of $L^*_{\rm Ly\alpha}$ and ϕ^* with the fixed value of $\alpha = -1.5$. Figure 10 shows error contours of the Schechter parameters of our $z = 7.3$ Lyα LF, together with those of $z = 6.6$ LF (Ouchi et al. 2010). Our measurements indicate that the Schechter parameters of $z = 7.3$ LF are different from those of $z = 6.6$ Lyα LF, and that the Lyα LF decreases from $z = 6.6$ to 7.3 at the $> 90\%$ confidence level. Because our $z = 7.3$ Lyα LF is derived with the same procedures as the $z = 6.6$ Lyα LF (Ouchi et al. 2010), one expects no systematic errors raised by the analysis technique for the comparison of the $z = 6.6$ and 7.3 results. From this aspect, it is reliable that the Lyα LF declines from $z = 6.6$ to 7.3 significantly. Here, we also discuss the possibilities of the LF decrease mimicked by our sample biases. In section 3.1, we assume that there is no contamination in our $z = 7.3$ LAE sample. If there exist some contamination sources, the $z = 7.3$ Lyα LF corrected for contamination should fall below the present estimate of the $z = 7.3$ Lyα LF. In this case, our conclusion of the significant LF decrease is even strengthened. In Section 2.3, we define

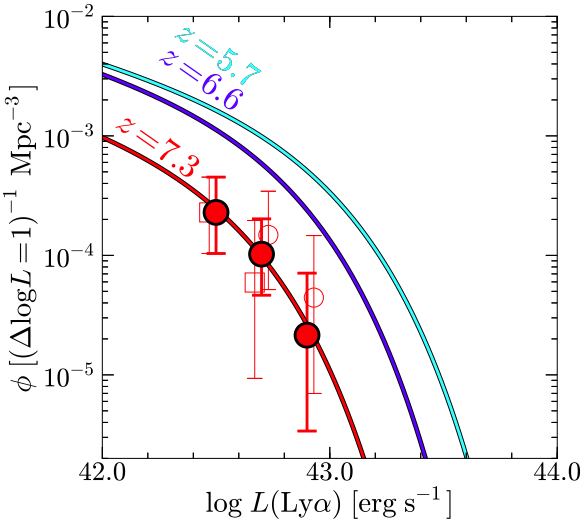

Figure 9. Evolution of Lyα LF at $z = 5.7 - 7.3$. The red filled circles are the best estimates of our $z = 7.3$ Lyα LF from the data of entire fields. The red open circles and squares denote our $z = 7.3$ Lyα LFs derived with the data of two independent fields of SXDS and COSMOS, respectively. The red curve is the best-fit Schechter function for the best estimate of our $z = 7.3$ Lyα LF. The cyan and blue curves are the best-fit Schechter functions of the Lyα LFs at $z = 5.7$ and 6.6 obtained by Ouchi et al. (2008) and Ouchi et al. (2010), respectively.

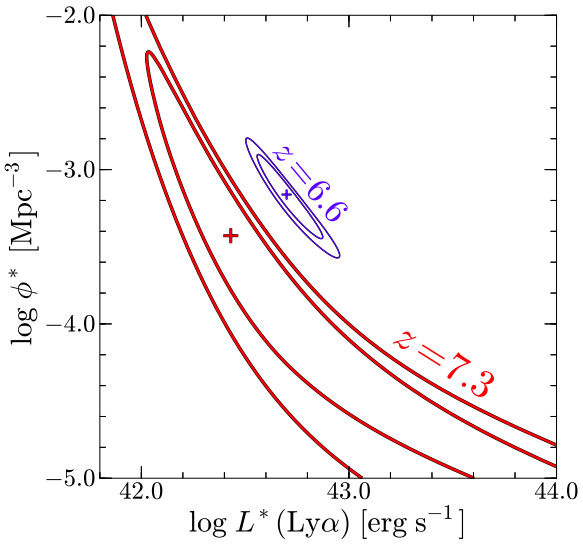

Figure 10. Error contours of Schechter parameters, $L^*_{\rm Ly\alpha}$ and ϕ^*. The red contours represent our Lyα LF at $z = 7.3$, while the blue contours denote the one at $z = 6.6$ obtained by Ouchi et al. (2010). The inner and outer contours indicate the 68% and 90% confidence levels, respectively. The red and blue crosses show the best-fit Schechter parameters for the Lyα LFs at $z = 7.3$ and 6.6, respectively.

the selection criterion of the rest-frame Lyα equivalent width of EW$_0 \gtrsim 0$Å for our $z = 7.3$ LAEs. This criterion of the EW$_0$ limit is slightly different from that of the LAEs for the $z = 6.6$ Lyα LF estimates. However, the EW$_0$ limit for the $z = 6.6$ LAEs is EW$_0 \gtrsim 14$Å (Ouchi et al. 2010) that is larger than our EW$_0$ limit of $z = 7.3$ LAEs. Because our EW$_0$ limit gives more $z = 7.3$ LAEs to our sample than that of $z = 6.6$ LAEs, the conclusion of the Lyα LF decrease from $z = 6.6$ to 7.3 is unchanged by the EW$_0$ limit.

Table 4
Best-fit Schechter Parameters and Lyα Luminosity Densities

Redshift	$L^*_{\rm Ly\alpha}$ (10^{42} erg s^{-1})	ϕ^* (10^{-4} Mpc^{-3})	$\rho^{\rm Ly\alpha\ a}$ (10^{39} erg s^{-1} Mpc^{-3})	$\rho^{\rm Ly\alpha,tot\ b}$ (10^{39} erg s^{-1} Mpc^{-3})	Reference
5.7	$6.8^{+3.0}_{-2.1}$	$7.7^{+7.4}_{-3.9}$	$3.6^{+3.1}_{-1.7}$	$9.2^{+6.6}_{-3.7}$	Ouchi et al. (2008)
6.6	$4.4^{+0.6}_{-0.6}$	$8.5^{+3.0}_{-2.2}$	$1.9^{+0.5}_{-0.4}$	$6.6^{+1.0}_{-0.8}$	Ouchi et al. (2010)
7.3	$2.7^{+8.0}_{-1.2}$	$3.7^{+17.6}_{-3.3}$	$0.31^{+0.19}_{-0.12}$	$1.8^{+3.8}_{-1.1}$	This study

[a] Lyα luminosity densities integrated down to the observation luminosity limit, $\log L_{\rm Ly\alpha} = 42.4$ erg s^{-1}, for all of the redshifts.
[b] Total Lyα luminosity densities integrated down to $L_{\rm Ly\alpha} = 0$.

Table 5
Lyα Luminosity Density Evolution

Redshift Range $z = z_1 - z_2$	$\rho^{\rm Ly\alpha}$ Evolution[a] $\rho^{\rm Ly\alpha}_{z_2}/\rho^{\rm Ly\alpha}_{z_1}$	$n(\rho)$[b]
$z = 5.7 - 6.6$	0.53 ± 0.37	$-5.0^{+4.2}_{-9.5}$
$z = 6.6 - 7.3$	0.16 ± 0.09	$-20.8^{+5.1}_{-9.4}$
$z = 5.7 - 7.3$	0.09 ± 0.07	$-11.2^{+2.7}_{-7.0}$

[a] Best-fit values of luminosity density ratio, $\rho^{\rm Ly\alpha}_{z_2}/\rho^{\rm Ly\alpha}_{z_1}$, where the indices of z_1 and z_2 denote redshifts.
[b] Power-law slope $n(\rho)$ defined with Equation (4).

4.3. *Accelerated Evolution of Lyα LF at $z \gtrsim 7$*

Figure 9 implies that the decrease of the Lyα LF from $z = 6.6$ to 7.3 is larger than that from $z = 5.7$ to 6.6, i.e., there is an accelerated evolution of the Lyα LF at $z = 6.6 - 7.3$. To evaluate this evolution quantitatively, we calculate the Lyα luminosity densities, $\rho^{\rm Ly\alpha}$, down to the common luminosity limit of $\log L_{\rm Ly\alpha} = 42.4$ erg s^{-1} reached by the observations for LAEs at $z = 5.7$, 6.6, and 7.3. Similarly, we estimate the total Lyα luminosity densities, $\rho^{\rm Ly\alpha,tot}$, that are integrated down to $L_{\rm Ly\alpha} = 0$ with the best-fit Schechter functions. Figure 11 presents the evolution of $\rho^{\rm Ly\alpha}$, and Table 4 summarizes the values of these Lyα luminosity densities at each redshift. Here, we use $\log(1+z)$ for the abscissa in Figure 11, because we compare the evolution of $\rho^{\rm Ly\alpha}$ with that of UV luminosity densities, $\rho^{\rm UV}$, derived by Oesch et al. (2013) who use $\log(1+z)$ (see Section 4.4). In this figure, we find a rapid decrease of the Lyα luminosity density at $z = 6.6 - 7.3$. To quantify this evolution, we calculate ratios of $\rho^{\rm Ly\alpha}_{z_2}/\rho^{\rm Ly\alpha}_{z_1}$ that are shown in Table 5, where z_1 and z_2 are redshifts. We fit the evolution of $\rho^{\rm Ly\alpha}_z$ to the power-law function,

$$\rho^{\rm Ly\alpha}_z \propto (1+z)^{n(\rho)}, \tag{4}$$

and obtain $n(\rho) = -5.0^{+4.2}_{-9.5}$ at $z = 5.7 - 6.6$ and $n(\rho) = -20.8^{+5.1}_{-9.4}$ at $z = 6.6 - 7.3$. Because these values of $n(\rho)$ are significantly different, we conclude that the Lyα LF evolves acceleratingly at $z \gtrsim 7$.

We also investigate pure-luminosity and number density evolution cases to test whether this rapid Lyα LF evolution is dominated by a L^* or ϕ^* decrease. These evolution cases are examined by the minimum χ^2 fitting. For example, to evaluate the pure-luminosity evolution from $z = 6.6$ to 7.3, we take a set of three parameters of $L^*_{z=6.6}$, $L^*_{z=7.3}/L^*_{z=6.6}$, and ϕ^*, where $L^*_{z=6.6}$ and $L^*_{z=7.3}/L^*_{z=6.6}$ are a Schechter parameter of L^* at $z = 6.6$ and a ratio of $z = 7.3$ L^* to $z = 6.6$ L^*, respectively. Here, ϕ^* is a common value in $z = 6.6$ and 7.3, and the Schechter parameter of α is fixed to -1.5. We prepare Schechter functions at $z = 6.6$ and 7.3 with the sets of three parameters, and search for the best-fit parameters that minimize χ^2 by the simultaneous fit of Schechter functions to $z = 6.6$ and 7.3 Lyα LFs. In this way, we obtain the best-fit parameter of $L^*_{z=7.3}/L^*_{z=6.6}$ that corresponds to a fraction of L^* for the pure-luminosity evolution between $z = 6.6$ and 7.3. Similarly, we estimate $L^*_{z=7.3}/L^*_{z=5.7}$ and $L^*_{z=6.6}/L^*_{z=5.7}$ at the redshift ranges. We also evaluate the pure-number density evolution with the ratios of ϕ^* in the same manner. We summarize the best-fit parameters for these pure-luminosity and number density evolutions in Table 6. Figure 12 shows the evolutions of the L^* and ϕ^* ratios from $z = 5.7$ to a redshift of z. In Figure 12, the shaded area denotes the L^* (and ϕ^*) evolution at $z = 5.7 - 6.6$ with the measurement uncertainties, and indicates the extrapolation of this evolutionary trend to $z = 7.3$. We find that the ratios of L^* and ϕ^* drop from $z = 6.6$ to 7.3 below the shaded area. Similar to Equation (4), we approximate the pure L^* and ϕ^* evolutions by power laws whose indices are $n(L^*)$ and $n(\phi^*)$:

$$\begin{aligned} L^*_z &\propto (1+z)^{n(L^*)} \\ \phi^*_z &\propto (1+z)^{n(\phi^*)}. \end{aligned} \tag{5}$$

We summarize the best-fit $n(L^*)$ and $n(\phi^*)$ values in Table 6. In either case of the pure-luminosity or number density evolution, the indices of n at $z = 6.6 - 7.3$ is significantly smaller than those at $z = 5.7 - 6.6$. These results are consistent with our conclusion of the accelerated evolution of the Lyα LF at $z \gtrsim 7$. The χ^2 values are comparable for the pure-luminosity and number density evolution cases (see Table 6), although the χ^2 values of the pure-luminosity evolution are slightly smaller than those of the pure-number density evolution. The available Lyα LF data do not have accuracies to discuss the dominant component of the evolution at $z = 5.7 - 7.3$. Nevertheless, if we assume the Lyα LF evolution is dominated by a pure L^* evolution whose χ^2 values are smaller than those of a pure ϕ^* evolution, we find that, in the pure L^* evolution, the decreases of the Lyα LF are 30% ($= [1 - L^*_{z=6.6}/L^*_{z=5.7}] \times 100$) and 70% ($= [1 - L^*_{z=7.3}/L^*_{z=5.7}] \times 100$) at $z = 5.7 - 6.6$ and $z = 5.7 - 7.3$, respectively. In other words, the typical LAE has gotten brighter by 1.4 times from $z = 6.6$ to 5.7 and 3.3 times from $z = 7.3$ to 5.7.

4.4. *Implications from the Accelerated Evolution of Lyα LF*

In Section 4.3, we find that the Lyα LF shows the accelerated evolution at a redshift beyond $z \sim 7$. We refer to the redshift starting the rapid decrease of the Lyα luminosity den-

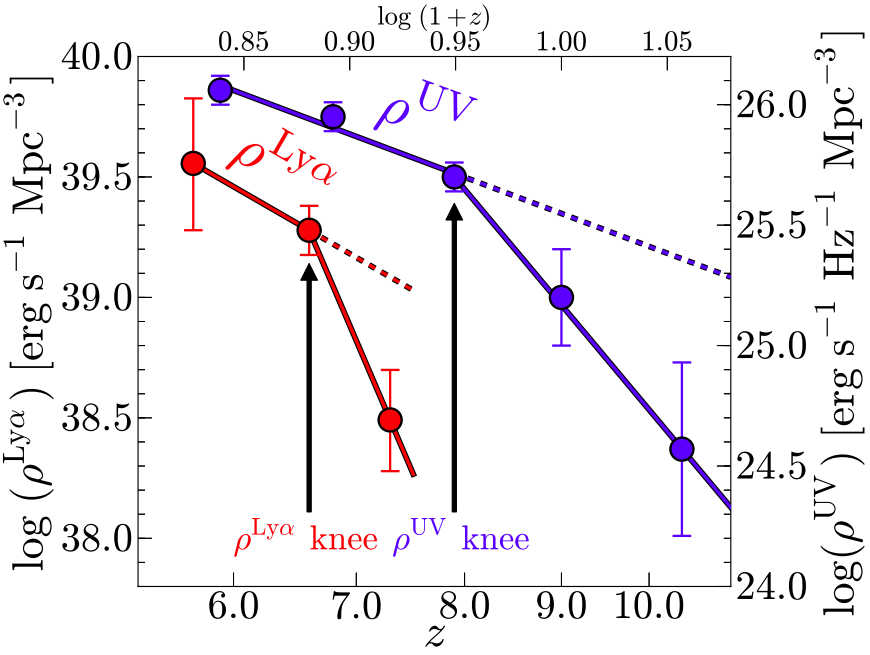

Figure 11. Evolution of Lyα and UV luminosity densities. The red circles are the Lyα luminosity densities obtained by this study, Ouchi et al. (2010), and Ouchi et al. (2008) for $z = 7.3$, 6.6, and 5.7, respectively. The blue circles are the UV luminosity densities given by Bouwens et al. (2014) for $z = 5.9$, 6.8, 7.9, and 10.4, and Ellis et al. (2013) for $z = 9.0$. The left ordinate axis is referred for the Lyα luminosity densities, and the right ordinate axis is for the UV luminosity densities. The Lyα luminosity density starts evolving acceleratingly at $z \sim 7$, while the UV luminosity density rapidly decreases at $z \sim 8$ and beyond. The $\rho^{Ly\alpha}$ and ρ^{UV} knees are indicated with the arrows.

Table 6
Best-Fit Parameters for Pure-Luminosity and Number Density evolution Cases

Redshift Range	$L^*_{Ly\alpha}$ Evolution[a]			ϕ^* Evolution[d]		
$z_1 - z_2$	$L^*_{z_2}/L^*_{z_1}$	$\chi^2(L^*)$[b]	$n(L^*)$[c]	$\phi^*_{z_2}/\phi^*_{z_1}$	$\chi^2(\phi^*)$[e]	$n(\phi^*)$[f]
$z = 5.7 - 6.6$	$0.70^{+0.09}_{-0.06}$	4.2	$-2.8^{+1.0}_{-0.7}$	$0.54^{+0.13}_{-0.09}$	4.7	$-4.9^{+1.7}_{-1.4}$
$z = 6.6 - 7.3$	$0.42^{+0.09}_{-0.07}$	1.6	$-9.8^{+2.2}_{-2.0}$	$0.18^{+0.09}_{-0.07}$	1.8	$-19.5^{+4.6}_{-5.6}$
$z = 5.7 - 7.3$	$0.30^{+0.07}_{-0.05}$	2.9	$-5.6^{+1.0}_{-0.9}$	$0.10^{+0.06}_{-0.04}$	3.4	$-10.8^{+2.2}_{-2.4}$

[a] Best-fit value of $L^*_{z_2}/L^*_{z_1}$, where the indices of z_1 and z_2 indicate redshifts.
[b] χ^2 for the best-fit $L^*_{z_2}/L^*_{z_1}$.
[c] Power-law slope $n(L^*)$ of Equation (5) for pure-luminosity evolution case.
[d] Best-fit value of $\phi^*_{z_2}/\phi^*_{z_1}$.
[e] χ^2 for the best-fit $\phi^*_{z_2}/\phi^*_{z_1}$.
[f] Power-law slope $n(\phi^*)$ of Equation (5) for pure-number density evolution case.

sity as "$\rho^{Ly\alpha}$ knee" that is indicated in Figure 11. In contrast with this evolution of the Lyα LF, there is no such a rapid decrease in the UV LF at $z \sim 7$, but only at $z > 8$, if any (Oesch et al. 2013; Bouwens et al. 2014). Figure 11 compares the evolution of $\rho^{Ly\alpha}$ (red symbols) and ρ^{UV} (blue symbols). Although the rapid decrease of the UV LF at $z > 8$ is still an open question (see, e.g., Ellis et al. 2013; Robertson et al. 2013), we refer to the redshift starting this possible rapid decrease of the UV LF as "ρ^{UV} knee". Again, there is a significant redshift difference between $\rho^{Ly\alpha}$ and ρ^{UV} knees (Figure 11). Because the evolution of ρ^{UV} correlates with the cosmic star-formation rate (SFR) history, the accelerated evolution of the Lyα LF found at $z \sim 7$ is not originated from a rapid decrease of the SFR density. To explain this accelerated evolution of the Lyα LF, there should exist physical mechanisms related to the Lyα production and escape processes. The simple interpretation of the Lyα LF decrease is that the Lyα damping wing of IGM given by cosmic reionization absorbs Lyα of galaxies strongly towards high redshifts. Here, we first investigate this simple scenario of cosmic reionization in Sections 4.4.1-4.4.2, and then discuss the physical origin of the accelerated evolution of the Lyα LF with various possible scenarios in Section 4.4.3.

4.4.1. *Constraints on x_{HI} at $z = 7.3$*

In Sections 4.4.1-4.4.2, we discuss the simple scenario of cosmic reionization that contributes to the accelerated evolution of the Lyα LF. We define $T^{IGM}_{Ly\alpha,z}$ as a Lyα transmission through IGM at a redshift of z, and calculate $T^{IGM}_{Ly\alpha,z=7.3}/T^{IGM}_{Ly\alpha,z=5.7}$ to estimate x_{HI} at $z = 7.3$. Because cosmic reionization has been completed at $z = 5.7$ (Fan et al.

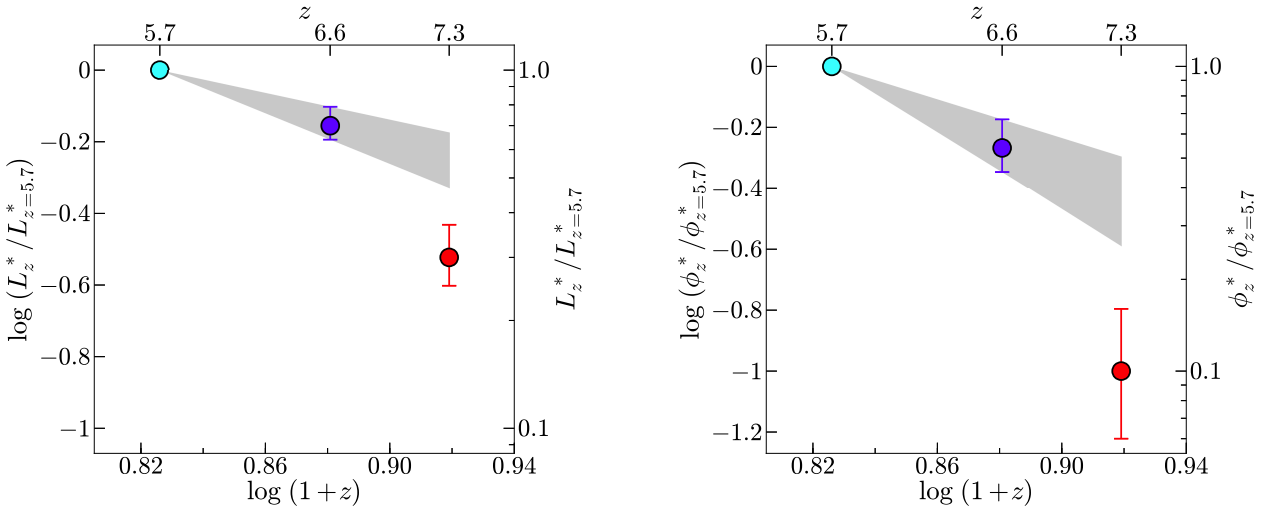

Figure 12. $L^*_{\rm Ly\alpha}$ and ϕ^* as a function of redshift for the cases of pure-luminosity evolution (left panel) and pure-number density evolution (right panel). For the both cases, the values of $z = 5.7$ are used for the normalization. The gray shades denote the L^* or ϕ^* evolution at $z = 5.7 - 6.6$ with the uncertainties, and these evolutionary trends are extrapolated to $z = 7.3$.

2006), the Lyα damping wing absorption of IGM is negligible at $z = 5.7$.

Section 4.3 presents the estimates of the Lyα luminosity densities from the Lyα LFs of Ouchi et al. (2008) and this study at $z = 5.7$ and 7.3, respectively (Table 4). There are two estimates of the Lyα luminosity densities, the observed Lyα luminosity density, $\rho^{\rm Ly\alpha}$, and the total one, $\rho^{\rm Ly\alpha,tot}$. Ouchi et al. (2010) calculate these two Lyα luminosity densities with their data and confirm that the ratio of these different estimates agree within the error bars (see Figure 19 of Ouchi et al. 2010). Thus, we adopt the total Lyα luminosity density for our fiducial results for cosmic reionization, which include no systematic bias from observations. With the values shown in Table 4, we obtain $\rho^{\rm Ly\alpha,tot}_{z=7.3}/\rho^{\rm Ly\alpha,tot}_{z=5.7} = 0.20$.

Because the Lyα LF evolution is made not only by cosmic reionization, but also by the SFR change of galaxy evolution, we subtract the effect of the SFR density evolution from the Lyα luminosity density evolution. An SFR of galaxy is correlated with the UV luminosity. The UV luminosity of $z = 7.3$ LAE in principle can be estimated by the subtraction of the Lyα line flux from the z'-band flux. However, we cannot derive the reliable UV luminosities from our data. This is because there exist the large uncertainties of the z'-band magnitude and the contamination of unknown amount of IGM absorption that make a significant bias in the estimate of the UV continuum as demonstrated in the simulations of Shimasaku et al. (2006). To derive a reliable UV LF of $z \gtrsim 6$ LAEs, one needs deep near-infrared data, such as J and H images, which cover the continuum emission longward of the Lyα line for most of LAEs, but no such data are available for LAE studies, to date. Since we cannot derive a reliable UV LF of $z = 7.3$ LAE from our data, we quantify $\rho^{\rm UV}$ at $z = 5.7 - 7.3$ given by the other observations. We use $\rho_{\rm UV}$ measured with the samples of dropout galaxies (Bouwens et al. 2009, 2011), and estimate $\rho^{\rm UV}$ at $z = 5.7$ and 7.3 by the interpolation of this evolution. We, thus, obtain $\rho^{\rm UV}_{z=7.3}/\rho^{\rm UV}_{z=5.7} = 0.70$.

Following the procedure of Ouchi et al. (2010), we estimate $T^{\rm IGM}_{{\rm Ly\alpha},z=7.3}/T^{\rm IGM}_{{\rm Ly\alpha},z=5.7}$ and $x_{\rm HI}$. The value of $\rho^{\rm Ly\alpha}$ is given by

$$\rho^{\rm Ly\alpha} = \kappa\, T^{\rm IGM}_{\rm Ly\alpha}\, f^{\rm esc}_{\rm Ly\alpha}\, \rho^{\rm UV}, \tag{6}$$

where κ is a factor converting from UV to Lyα luminosities, which depends on stellar population. $f^{\rm esc}_{\rm Ly\alpha}$ is a fraction of Lyα emission escape from a galaxy through the inter-stellar medium (ISM) absorption including galactic neutral hydrogen and dust attenuation. With Equation (6), $T^{\rm IGM}_{{\rm Ly\alpha},z=7.3}/T^{\rm IGM}_{{\rm Ly\alpha},z=5.7}$ is written as

$$\frac{T^{\rm IGM}_{{\rm Ly\alpha},z=7.3}}{T^{\rm IGM}_{{\rm Ly\alpha},z=5.7}} = \frac{\kappa_{z=5.7}}{\kappa_{z=7.3}} \frac{f^{\rm esc}_{{\rm Ly\alpha},z=5.7}}{f^{\rm esc}_{{\rm Ly\alpha},z=7.3}} \frac{\rho^{\rm Ly\alpha,tot}_{z=7.3}/\rho^{\rm Ly\alpha,tot}_{z=5.7}}{\rho^{\rm UV}_{z=7.3}/\rho^{\rm UV}_{z=5.7}}. \tag{7}$$

Assuming that the stellar population of LAEs is the same at $z = 5.7$ and 7.3 (i.e., $\kappa_{z=5.7}/\kappa_{z=7.3} = 1$), and the physical state of ISM is not evolved at $z = 5.7 - 7.3$ (i.e., $f^{\rm esc}_{{\rm Ly\alpha},z=5.7}/f^{\rm esc}_{{\rm Ly\alpha},z=7.3} = 1$), we obtain

$$\frac{T^{\rm IGM}_{{\rm Ly\alpha},z=7.3}}{T^{\rm IGM}_{{\rm Ly\alpha},z=5.7}} = \frac{\rho^{\rm Ly\alpha,tot}_{z=7.3}/\rho^{\rm Ly\alpha,tot}_{z=5.7}}{\rho^{\rm UV}_{z=7.3}/\rho^{\rm UV}_{z=5.7}}. \tag{8}$$

From the ratios of the Lyα and UV luminosity densities described above, we estimate $T^{\rm IGM}_{{\rm Ly\alpha},z=7.3}/T^{\rm IGM}_{{\rm Ly\alpha},z=5.7}$ to be 0.29.

We use theoretical models to constrain $x_{\rm HI}$ at $z = 7.3$ with our estimates of $T^{\rm IGM}_{{\rm Ly\alpha},z=7.3}/T^{\rm IGM}_{{\rm Ly\alpha},z=5.7} = 0.29$. In the analytic model of Santos (2004), the Lyα transmission fraction of IGM is related to $x_{\rm HI}$ in two cases of no galactic wind and a galactic outflow that give shifts of Lyα line from a systemic velocity by 0 and 360 km/s, respectively. The value of $T^{\rm IGM}_{{\rm Ly\alpha},z=7.3}/T^{\rm IGM}_{{\rm Ly\alpha},z=5.7} = 0.29$ corresponds to $x_{\rm HI} \sim 0.0$ and ~ 0.8 in the former and the latter case, respectively. Because recent studies have reported that the Lyα line emission of LAE at $z = 2.2$ is redshifted by ~ 200 km/s (Hashimoto et al. 2013; Shibuya et al. 2014), we take $x_{\rm HI} \sim 0.5$ that is the $x_{\rm HI}$ value interpolated by the Lyα velocity shift in Figure 25 of Santos (2004). McQuinn et al. (2007) predict Lyα LFs for various $x_{\rm HI}$ values with radiative transfer simulations. By the comparison of our Lyα LF with these simulation results in Figure 4 of McQuinn et al. (2007), we obtain $x_{\rm HI} \sim 0.7$. In the models of Dijkstra et al. (2007a,b), the Lyα transmission

fraction of IGM is related to the size of typical ionized bubbles, and Furlanetto et al. (2006) predict $x_{\rm HI}$ from the size of the ionized bubble with the analytic model. Based on Figure 6 of Dijkstra et al. (2007b), our estimates of the Lyα transmission fraction of IGM at $z = 5.7 - 7.3$ suggest that the typical size of the ionized bubble is very small, ~ 2 comoving Mpc, and the estimated neutral hydrogen fraction is ~ 0.6 from the top panel of Figure 1 of Furlanetto et al. (2006). Based on these results of $x_{\rm HI}$, we conclude the neutral hydrogen fraction is relatively high, $x_{\rm HI} = 0.3 - 0.8$ at $z = 7.3$ that includes the uncertainties of the various model predictions and the Lyα transmission fraction estimated from the observations.

In Figure 13, we plot our estimate of $x_{\rm HI}$ at $z = 7.3$, and compare it with those from the previous studies. The measurements of the Lyα LF imply $x_{\rm HI} < 0.63$ at $z = 7.0$ (Ota et al. 2010), and this result is consistent with our estimate of $x_{\rm HI} = 0.3 - 0.8$ at $z = 7.3$. The studies of Lyα emitting fraction by Pentericci et al. (2011), Schenker et al. (2012), Ono et al. (2012), Treu et al. (2012), Caruana et al. (2012, 2014), Pentericci et al. (2014), and Schenker et al. (2014) indicate $x_{\rm HI} \gtrsim 0.5$ at $z \sim 7$, and these estimates are also comparable with ours within the uncertainties. Moreover, the Lyα damping wing absorption of QSO continuum suggests $x_{\rm HI} \gtrsim 0.1$ at $z = 7.1$ (Mortlock et al. 2011; Bolton et al. 2011) that is, again, consistent with our estimate.

In Section 4.2, we find that the decrease of the Lyα LF at $z = 6.6 - 7.3$ is larger than that at $z = 5.7 - 6.6$. This accelerated evolution can be also found in Figure 13, albeit with the large uncertainties, by the comparison of our $z = 7.3$ result (red filled circle) with the strongest upper limit of $x_{\rm HI}$ from the previous $z = 6.6$ result (blue filled diamond). While we find that the Lyα LF decreases from $z = 6.6$ to 7.3 at the $> 90\%$ confidence level, the difference of the $x_{\rm HI}$ estimates between $z = 6.6$ and 7.3 is only within the 1σ level that is less significant than the Lyα LF evolution result. This is because the error bar of $x_{\rm HI}$ at $z = 7.3$ is not only from the uncertainties of the Lyα LF estimates, but also from the errors of the UV LF measurements and the variance of the theoretical model results.

It is implied that the amount of IGM neutral hydrogen may increase acceleratingly at $z \sim 7$. However, the results of the $x_{\rm HI}$ evolution are based on various assumptions that should be examined carefully. In Section 4.4.1, we assume $f^{\rm esc}_{{\rm Ly}\alpha,z=5.7}/f^{\rm esc}_{{\rm Ly}\alpha,z=7.3} = 1$. Observational studies show that the Lyα escape fraction of LAEs increases from $z \sim 0$ to ~ 6, i.e., $f^{\rm esc}_{{\rm Ly}\alpha,z=0}/f^{\rm esc}_{{\rm Ly}\alpha,z=6} < 1$ (Ouchi et al. 2008; Hayes et al. 2011; see also Ono et al. 2010). If this trend continues to $z = 7.3$, the intrinsic Lyα escape fraction with no IGM absorption would be $f^{\rm esc}_{{\rm Ly}\alpha,z=5.7}/f^{\rm esc}_{{\rm Ly}\alpha,z=7.3} < 1$. In this case, we obtain the value of $T^{\rm IGM}_{{\rm Ly}\alpha,z=7.3}/T^{\rm IGM}_{{\rm Ly}\alpha,z=5.7}$ is smaller than our estimate above (see Equation 7) and an $x_{\rm HI}$ estimate higher than our result of $x_{\rm HI} = 0.3 - 0.8$ at $z = 7.3$.

4.4.2. *Comparison with Optical Depth of Thomson Scattering*

In this section, we investigate whether the relatively high value of our $x_{\rm HI}$ estimate can explain the Thomson scattering optical depth, $\tau_{\rm el}$, measurements given by *WMAP* and *Planck*. Because one needs to know $x_{\rm HI}$ evolution at $z = 0 - 1100$ to derive $\tau_{\rm el}$, we use three models of the $x_{\rm HI}$ evolution (Choudhury et al. 2008) that cover typical scenarios of the early and relatively-late cosmic reionization history. We refer to these three $x_{\rm HI}$ evolution models as models A, B, and C corresponding to the minimum halo masses for reionization sources that are $\sim 10^9$, $\sim 10^8$, and $\sim 5 \times 10^5\ M_\odot$, respectively, at $z = 6$ in the semi-analytic models of Choudhury et al. (2008). We present the $x_{\rm HI}$evolution of models A, B, and C in Figure 13, and $\tau_{\rm el}$ as a function of redshift for these models in Figure 14. In Figure 14, the hatched and gray regions represent the 1σ range of $\tau_{\rm el}$ measured by *WMAP* and *WMAP+Planck*, respectively. While models A and B are consistent with our $x_{\rm HI}$ estimate at $z = 7.3$ in Figure 13, the models A and B fall far below the $\tau_{\rm el}$ measurements of *WMAP* and *WMAP+Planck* in Figure 14. These results require reionization that proceeds at an epoch earlier than the models A and B. The model C is such an early reionization model that just agrees with the lower end of the error of our

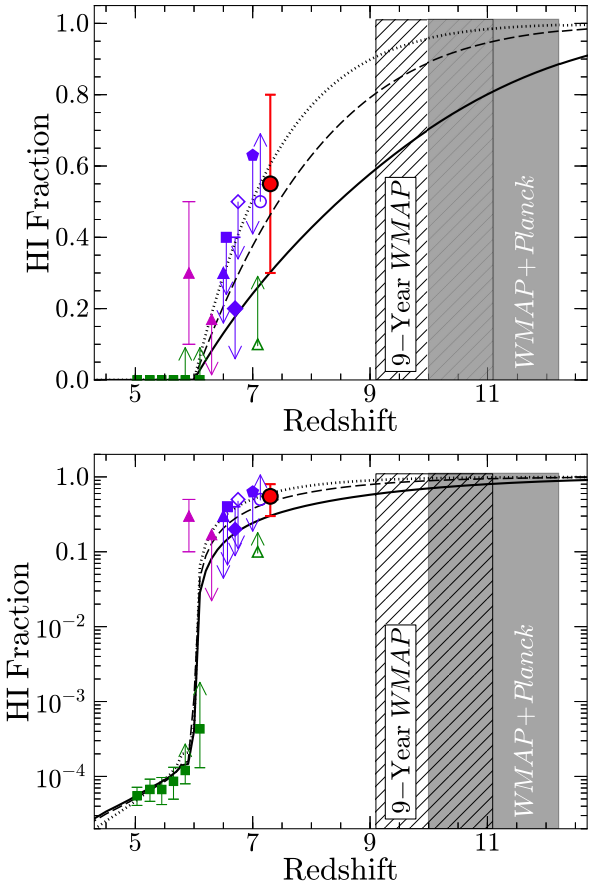

Figure 13. Evolution of neutral hydrogen fraction of IGM. Top and bottom panels are the same plots, but with the ordinate axes of linear and logarithmic scales, respectively. The red filled circle is the $x_{\rm HI}$ estimate from our Lyα LF at $z = 7.3$. The blue filled triangle, square, diamond, and pentagon denote the $x_{\rm HI}$ values from the Lyα LF evolution presented in Malhotra & Rhoads (2004), Kashikawa et al. (2011), Ouchi et al. (2010), and Ota et al. (2010), respectively. The blue open diamond and circle indicate the $x_{\rm HI}$ constraints given by the clustering of LAEs (Ouchi et al. 2010) and the Lyα emitting galaxy fraction (Pentericci et al. 2011; Schenker et al. 2012; Ono et al. 2012; Treu et al. 2012; Caruana et al. 2012, 2014; Pentericci et al. 2014; Schenker et al. 2014), respectively. The magenta filled triangles show the $x_{\rm HI}$ measurements from the optical afterglows of GRBs (Totani et al. 2006, 2014). The green filled squares and open triangle are the $x_{\rm HI}$ constraints provided from the GP test of QSOs (Fan et al. 2006) and the size of QSO near zone (Mortlock et al. 2011; Bolton et al. 2011), respectively. The hatched and gray regions represent the 1σ ranges for the instantaneous reionization redshifts obtained by nine-year *WMAP* (Hinshaw et al. 2013; Bennett et al. 2013) and *WMAP+Planck* (Planck Collaboration et al. 2013), respectively. The doted, dashed and solid lines show the models A, B, and C, respectively (Choudhury et al. 2008).

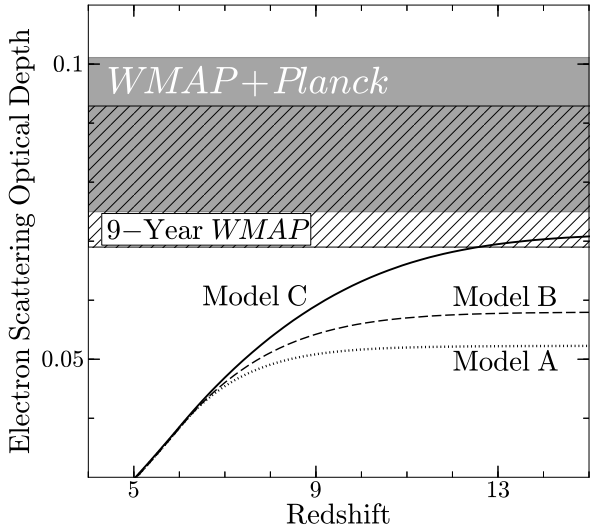

Figure 14. Evolution of Thomson scattering optical depth, $\tau_{\rm el}$. The hatched and gray regions indicate the 1σ ranges of the $\tau_{\rm el}$ measurements of $\tau_{\rm el}= 0.081 \pm 0.012$ and $\tau_{\rm el}= 0.089^{+0.012}_{-0.014}$ obtained by nine-year *WMAP* (Hinshaw et al. 2013; Bennett et al. 2013) and *WMAP+Planck* (Planck Collaboration et al. 2013), respectively. The doted, dashed, and solid curves represent the models A, B, and C, respectively (Choudhury et al. 2008).

$x_{\rm HI}$ estimate at $z = 7.3$ in Figure 13. However, the model C is barely consistent with the *WMAP* result within the 1σ error in Figure 14. Moreover, in Figure 14, the $\tau_{\rm el}$ value from *WMAP+Planck* is higher than the one of model C beyond the uncertainty. Thus, there is a possible tension between our estimate of high $x_{\rm HI}$ and the CMB measurements of high $\tau_{\rm el}$. A similar tension between $\tau_{\rm el}$ and galaxy observation results is also claimed by Robertson et al. (2010) who discuss UV luminosities of reionization sources that are based on observational quantities independent from the Lyα LFs of our study.

4.4.3. *Physical Origin of the Accelerated Evolution of Lyα LF*

The physical origin of the accelerated Lyα LF evolution could be something other than the rapid increase of the neutral hydrogen at $z \gtrsim 7$, because the $\tau_{\rm el}$ measurements have a tension with the high $x_{\rm HI}$ value that is estimated with our Lyα LF under the assumption that the Lyα LF evolution is given by the combination of cosmic reionization and cosmic SFR density evolution. Similarly, large values of $x_{\rm HI}$ estimates at $z \simeq 6 - 7$ are obtained from the Lyα damping wing absorption techniques with LAEs (Kashikawa et al. 2006, 2011; Ota et al. 2008, 2010; Ouchi et al. 2010; Shibuya et al. 2012), LBGs (Pentericci et al. 2011; Schenker et al. 2012; Ono et al. 2012; Treu et al. 2012; Caruana et al. 2012, 2014; Pentericci et al. 2014; Schenker et al. 2014), QSOs (Bolton et al. 2011), and GRBs (Totani et al. 2014). Recent theoretical studies suggest a few physical pictures that explain the $\tau_{\rm el}$ measurements and the large $x_{\rm HI}$ estimates given by the Lyα damping wing absorption measurements. The first picture is the presence of clumpy neutral hydrogen clouds in ionized bubbles at the end of reionization epoch. Lyα line and UV continuum from objects would be attenuated by a number of optically thick absorption systems that have large HI column densities such as Lyman limit systems (Bolton & Haehnelt 2013; Xu et al. 2014). The absorption systems of the clumpy HI clouds do not contribute to the volume-limited value of $x_{\rm HI}$ significantly, but to the attenuation of Lyα-line and UV-continuum emitted from objects. Interestingly, recent ALMA observations report a possible HI cloud emitting [CII]158μm near a star-forming galaxy at $z = 6.6$ (Ono et al. 2014), supporting this physical picture. If this picture is correct, our finding of the accelerated Lyα LF evolution indicates that the number of such clumpy HI clouds rapidly increases at $z \gtrsim 7$. The second picture is the increase of ionizing photon escape fraction towards high-z (Dijkstra et al. 2014). Lyα photons are produced by recombination following photoionization in ionized gas of a galaxy. The more the ionizing photons escape from the galaxy, the smaller an amount of recombination is. Under the significant escape of the ionizing photons, Lyα emission is not efficiently produced by ionized clouds in a galaxy. This picture reconciles with the increase of the ionizing photon escape fraction suggested by Nakajima & Ouchi (2014) from the ionization parameter evolution. If this picture is correct, the accelerated Lyα LF evolution would suggest either the sudden decrease of the gas covering fraction of galaxies or the boosting of the ionization parameter that would make density-bounded clouds in galaxies. However, in this picture, the high $x_{\rm HI}$ values given by the UV-continuum studies of QSOs and GRBs are not explained. Additional physical mechanisms would be required for these $x_{\rm HI}$ results of the UV-continuum studies.

Another possibility is that the tension between the $x_{\rm HI}$ estimates and $\tau_{\rm el}$ would not exist, because the uncertainty of the $x_{\rm HI}$ estimates are very large (Figure 13). In fact, the tension is found at the significance level only beyond ~ 1 sigma. It is not clear whether the tension is a hint for the discrepancy between the $x_{\rm HI}$ and $\tau_{\rm el}$ estimates. One of the dominant factors of the $x_{\rm HI}$ uncertainty is the error of the Lyα LFs, which is largely caused by the statistical errors due to the small LAE samples. To obtain a large sample of LAEs, it is necessary to carry out narrowband imaging observations in survey fields significantly wider than this study. One promising project is the Subaru/Hyper Suprime-Cam (HSC) survey that will complete 30 deg^2 and 3.5 deg^2 narrowband observations for LAEs at $z = 5.7 - 6.6$ and $5.7 - 7.3$, respectively, with the depth comparable with those accomplished by the present Subaru surveys. With the strong constraint of $x_{\rm HI}$ given by the HSC survey, we will address the problem whether the tension is a discrepancy between $x_{\rm HI}$ and $\tau_{\rm el}$ estimates and a new physical picture is really needed.

5. SUMMARY

We have conducted the ultra-deep Subaru/Suprime-Cam imaging survey for $z = 7.3$ LAEs with our custom narrowband filter, *NB101*, that has a sharp bandpass for a high sensitivity of faint line detection. We have observed a total of $\simeq 0.5$ deg^2 sky of SXDS and COSMOS fields with the integration times of 36.3 and 69.5 hours, respectively. We have reached the 5σ limiting luminosity of $L({\rm Ly}\alpha) \sim 2.4 \times 10^{42}$ erg s^{-1}, which is about 4 times deeper than those achieved by the previous Subaru studies for $z \gtrsim 7$ LAEs and comparable with the luminosity limits of the previous Subaru $z = 3.1 - 6.6$ LAE surveys. Our observations allow us to derive the Lyα LF at $z = 7.3$ with the unprecedented accuracy, and to examine the Lyα LF evolution from $z = 6.6$ to 7.3 reliably. The major results of our study are listed below.

1. We identify three and four LAEs in SXDS and COSMOS fields, respectively. These numbers are surprisingly small, because we expect to find a total of ~ 65 LAEs by our survey in the case of no evolution of

Lyα LF from $z = 6.6$ to 7.3. We derive the Lyα LF at $z = 7.3$ with our data, carefully evaluating uncertainties of Poisson statistics and cosmic variance. We fit Schechter functions to our Lyα LF, and obtain the best-fit Schechter parameters, $L^*_{\rm Ly\alpha} = 2.7^{+8.0}_{-1.2} \times 10^{42}$ erg s^{-1} and $\phi^* = 3.7^{+17.6}_{-3.3} \times 10^{-4}$ Mpc^{-3} with a fixed $\alpha = -1.5$.

2. We compare our Lyα LF with the previous measurements of the Lyα LF at $z \simeq 7.3$. Our Lyα LF measurements are consistent with those of the previous Subaru and VLT studies, but significantly smaller than those of the 4m-telescope observations. The significant differences of the Lyα LF between the 4m-telescope programs and Subaru+VLT studies including ours could not be explained by cosmic variance. It is possible that the 4m-telescope results are derived with the highly contaminated LAE samples, as suggested by the recent spectroscopic follow-up observations that find no emission lines in the LAEs of the 4m-telescope samples.

3. We identify the decrease of the Lyα LF from $z = 6.6$ to 7.3 significantly at the $> 90\%$ confidence level in the Schechter function parameter space (Figure 10), comparing with the Lyα LFs at $z = 6.6$ obtained from the largest LAE sample of Subaru survey with the estimates of the cosmic variance uncertainties. Using our Lyα LFs at $z = 7.3$ and the Subaru results at $z = 5.7 - 6.6$, we find the rapid decrease of the Lyα LF indicated by the evolution of the Lyα luminosity density ratios (Figure 11). Approximating the evolution of the Lyα luminosity density with the power-law function, $(1+z)^{n(\rho)}$, we obtain $n(\rho) = -5.0^{+4.2}_{-9.5}$ at $z = 5.7 - 6.6$ and $n(\rho) = -20.8^{+5.1}_{-9.4}$ at $z = 6.6 - 7.3$. Because these values of $n(\rho)$ are significantly different beyond the uncertainties, we conclude that there is the accelerated evolution of the Lyα LF at $z \gtrsim 7$.

4. Because no accelerated evolution of the UV-continuum LF or the cosmic star-formation rate (SFR) is found at $z \sim 7$, but suggested only at $z > 8$, if any (Oesch et al. 2013; Bouwens et al. 2014), this accelerated Lyα LF evolution is explained by physical mechanisms different from pure SFR decreases of galaxies but related to the Lyα production and escape in the process of cosmic reionization. We discuss the simple scenario of cosmic reionization that contributes to the accelerated evolution of the Lyα LF. Subtracting the effect of the galaxies' SFR evolution from the decrease of the Lyα luminosity density, we estimate the ratio of Lyα transmission of IGM to be $T^{\rm IGM}_{{\rm Ly}\alpha,z=7.3}/T^{\rm IGM}_{{\rm Ly}\alpha,z=5.7} = 0.29$. By the comparison of theoretical models, we obtain $x_{\rm HI} = 0.3 - 0.8$ whose large uncertainty includes the variance of the theoretical model predictions. Although this result is consistent with previous $z \sim 7$ studies that use the Lyα damping wing absorption, there would exist a tension between the $x_{\rm HI}$ estimate and the Thomson scattering optical depth, $\tau_{\rm el}$, measurements from *WMAP* and *Planck* at the significance level only beyond ~ 1 sigma. If this tension is a hint for the discrepancies between the $x_{\rm HI}$ and $\tau_{\rm el}$ estimates, these results support new physical pictures such as the clumpy neutral gas cloud absorption and the increase of the ionizing photon escape fraction suggested by recent theoretical studies.

We thank Martin Haehnelt, Koki Kakiichi, Lucia Guaita, Masayuki Umemura, Kentaro Nagamine, and Masao Hayashi for useful comments and discussions. We are grateful to Tirthankar Roy Choudhury for providing his data. We appreciate Carnegie Observatories and the director, Wendy Freedman, who provided the fund for the *NB101* filter that was key for achieving our ultra-deep survey. This work was supported by World Premier International Research Center Initiative (WPI Initiative), MEXT, Japan, and KAKENHI (23244025) Grant-in-Aid for Scientific Research (A) through Japan Society for the Promotion of Science (JSPS). K.N. and S.Y. acknowledge the JSPS Research Fellowship for Young Scientists.

Facility: Subaru (Suprime-Cam)

REFERENCES

Bardeen, J. M., Bond, J. R., Kaiser, N., & Szalay, A. S. 1986, ApJ, 304, 15
Bennett, C. L., Larson, D., Weiland, J. L., et al. 2013, ApJS, 208, 20
Bertin, E. & Arnouts, S. 1996, A&AS, 117, 393
Bohlin, R. C., Colina, L., & Finley, D. S. 1995, AJ, 110, 1316
Bolton, J. S. & Haehnelt, M. G. 2013, MNRAS, 429, 1695
Bolton, J. S., Haehnelt, M. G., Warren, S. J., et al. 2011, MNRAS, 416, L70
Bouwens, R. J., Illingworth, G. D., Franx, M., et al. 2009, ApJ, 705, 936
Bouwens, R. J., Illingworth, G. D., Oesch, P. A., et al. 2011, ApJ, 737, 90
—. 2014, ArXiv e-prints, arXiv:1403.4295
Capak, P. et al. 2007, ApJS, 172, 99
Carroll, S. M., Press, W. H., & Turner, E. L. 1992, ARA&A, 30, 499
Caruana, J., Bunker, A. J., Wilkins, S. M., et al. 2012, MNRAS, 427, 3055
—. 2014, MNRAS, 443, 2831
Choudhury, T. R., Ferrara, A., & Gallerani, S. 2008, MNRAS, 385, L58
Clément, B., Cuby, J.-G., Courbin, F., et al. 2012, A&A, 538, A66
Cuby, J.-G., Hibon, P., Lidman, C., et al. 2007, A&A, 461, 911
Dijkstra, M., Lidz, A., & Wyithe, J. S. B. 2007a, MNRAS, 377, 1175
Dijkstra, M., Wyithe, J. S. B., & Haiman, Z. 2007b, MNRAS, 379, 253
Dijkstra, M., Wyithe, S., Haiman, Z., et al. 2014, MNRAS, 440, 3309
Ellis, R. S., McLure, R. J., Dunlop, J. S., et al. 2013, ApJ, 763, L7
Faisst, A. L., Capak, P., Carollo, C. M., et al. 2014, ApJ, 788, 87
Fan, X., Strauss, M. A., Becker, R. H., et al. 2006, AJ, 132, 117
Furlanetto, S. R., Zaldarriaga, M., & Hernquist, L. 2006, MNRAS, 365, 1012
Furusawa, H., Kosugi, G., Akiyama, M., et al. 2008, ApJS, 176, 1
Gehrels, N. 1986, ApJ, 303, 336
Grogin, N. A., Kocevski, D. D., Faber, S. M., et al. 2011, ApJS, 197, 35
Gunn, J. E. & Peterson, B. A. 1965, ApJ, 142, 1633
Gunn, J. E. & Stryker, L. L. 1983, ApJS, 52, 121
Hashimoto, T., Ouchi, M., Shimasaku, K., et al. 2013, ApJ, 765, 70
Hayes, M., Schaerer, D., Östlin, G., et al. 2011, ApJ, 730, 8
Hibon, P., Cuby, J.-G., Willis, J., et al. 2010, A&A, 515, A97
Hinshaw, G., Larson, D., Komatsu, E., et al. 2013, ApJS, 208, 19
Hu, E. M., Cowie, L. L., Barger, A. J., et al. 2010, ApJ, 725, 394
Hu, E. M., Cowie, L. L., Capak, P., et al. 2005, in IAU Colloq. 199: Probing Galaxies through Quasar Absorption Lines, ed. P. Williams, C.-G. Shu, & B. Menard, 363–368
Iye, M., Ota, K., Kashikawa, N., et al. 2006, Nature, 443, 186
Jiang, L., Bian, F., Fan, X., et al. 2013, ApJ, 771, L6
Kamata, Y., Miyazaki, S., Nakaya, H., et al. 2008, in Society of Photo-Optical Instrumentation Engineers (SPIE) Conference Series, Vol. 7021, Society of Photo-Optical Instrumentation Engineers (SPIE) Conference Series
Kashikawa, N., Shimasaku, K., Malkan, M. A., et al. 2006, ApJ, 648, 7
Kashikawa, N., Shimasaku, K., Matsuda, Y., et al. 2011, ApJ, 734, 119
Koekemoer, A. M., Faber, S. M., Ferguson, H. C., et al. 2011, ApJS, 197, 36
Krug, H. B., Veilleux, S., Tilvi, V., et al. 2012, ApJ, 745, 122
Lawrence, A., Warren, S. J., Almaini, O., et al. 2007, MNRAS, 379, 1599
Madau, P. 1995, ApJ, 441, 18
Malhotra, S. & Rhoads, J. E. 2004, ApJ, 617, L5
Matthee, J. J. A., Sobral, D., Swinbank, A. M., et al. 2014, MNRAS, 440, 2375
McQuinn, M., Hernquist, L., Zaldarriaga, M., et al. 2007, MNRAS, 381, 75
Miyazaki, S., Komiyama, Y., Sekiguchi, M., et al. 2002, PASJ, 54, 833
Mo, H. J. & White, S. D. M. 2002, MNRAS, 336, 112
Mortlock, D. J., Warren, S. J., Venemans, B. P., et al. 2011, Nature, 474, 616
Nakajima, K. & Ouchi, M. 2014, MNRAS, 442, 900
Oesch, P. A., Bouwens, R. J., Illingworth, G. D., et al. 2013, ApJ, 773, 75
Oke, J. B. 1974, ApJS, 27, 21

Ono, Y., Ouchi, M., Kurono, Y., & Momose, R. 2014, ArXiv e-prints, arXiv:1403.4360
Ono, Y., Ouchi, M., Mobasher, B., et al. 2012, ApJ, 744, 83
Ono, Y., Ouchi, M., Shimasaku, K., et al. 2010, ApJ, 724, 1524
Ota, K., Iye, M., Kashikawa, N., et al. 2008, ApJ, 677, 12
—. 2010, ApJ, 722, 803
Ouchi, M., Shimasaku, K., Akiyama, M., et al. 2008, ApJS, 176, 301
Ouchi, M., Shimasaku, K., Furusawa, H., et al. 2010, ApJ, 723, 869
Ouchi, M., Shimasaku, K., Okamura, S., et al. 2004, ApJ, 611, 660
Pentericci, L., Fontana, A., Vanzella, E., et al. 2011, ApJ, 743, 132
Pentericci, L., Vanzella, E., Fontana, A., et al. 2014, ArXiv e-prints, arXiv:1403.5466
Planck Collaboration et al. 2013, ArXiv e-prints, arXiv:1303.5076
Robertson, B. E., Ellis, R. S., Dunlop, J. S., et al. 2010, Nature, 468, 49
Robertson, B. E., Furlanetto, S. R., Schneider, E., et al. 2013, ApJ, 768, 71
Santos, M. R. 2004, MNRAS, 349, 1137
Schechter, P. 1976, ApJ, 203, 297
Schenker, M. A., Ellis, R. S., Konidaris, N. P., & Stark, D. P. 2014, ArXiv e-prints, arXiv:1404.4632
Schenker, M. A., Stark, D. P., Ellis, R. S., et al. 2012, ApJ, 744, 179
Scoville, N., Aussel, H., Brusa, M., et al. 2007, ApJS, 172, 1
Shibuya, T., Kashikawa, N., Ota, K., et al. 2012, ApJ, 752, 114
Shibuya, T., Ouchi, M., Nakajima, K., et al. 2014, ApJ, 788, 74
Shimasaku, K., Kashikawa, N., Doi, M., et al. 2006, PASJ, 58, 313
Sobral, D., Best, P. N., Geach, J. E., et al. 2009, MNRAS, 398, L68
Tilvi, V., Rhoads, J. E., Hibon, P., et al. 2010, ApJ, 721, 1853
Totani, T., Aoki, K., Hattori, T., et al. 2014, PASJ, 66, 63
Totani, T., Kawai, N., Kosugi, G., et al. 2006, PASJ, 58, 485
Treu, T., Trenti, M., Stiavelli, M., et al. 2012, ApJ, 747, 27
Willis, J. P. & Courbin, F. 2005, MNRAS, 357, 1348
Willis, J. P., Courbin, F., Kneib, J.-P., & Minniti, D. 2008, MNRAS, 384, 1039
Xu, Y., Yue, B., Su, M., et al. 2014, ApJ, 781, 97
Yagi, M., Kashikawa, N., Sekiguchi, M., et al. 2002, AJ, 123, 66